Monthly Notices of the ROYAL ASTRONOMICAL SOCIETY

MNRAS **537,** 2850–2867 (2025) https://doi.org/10.1093/mnras/staf179
Advance Access publication 2025 January 29

Variety of disc wind-driven explosions in massive rotating stars – II. Dependence on the progenitor

Ludovica Crosato Menegazzi [1]★ Sho Fujibayashi,[1,2,3] Masaru Shibata,[1,4] Aurore Betranhandy[1] and Koh Takahashi[1,5]

[1] *Max Planck Institute for Gravitational Physics (Albert Einstein Institute), Am Mühlenberg 1, Potsdam D-14476, Germany*
[2] *Frontier Research Institute for Interdisciplinary Sciences, Tohoku University, Sendai 980-8578, Japan*
[3] *Astronomical Institute, Graduate School of Science, Tohoku University, Sendai 980-8578, Japan*
[4] *Center for Gravitational Physics and Quantum Information, Yukawa Institute for Theoretical Physics, Kyoto University, Kyoto 606-8502, Japan*
[5] *National Astronomical Observatory of Japan, National Institutes for Natural Science, 2-21-1 Osawa, Mitaka, Tokyo 181-8588, Japan*

Accepted 2025 January 25. Received 2025 January 24; in original form 2024 November 7

ABSTRACT

We assess the variance of supernova(SN)-like explosions associated with the core collapse of rotating massive stars into a black hole-accretion disc system under changes in the progenitor structure. Our model of the central engine evolves the black hole and the disc through the transfer of matter and angular momentum and includes the contribution of the disc wind. We perform two-dimensional, non-relativistic, hydrodynamics simulations using the open-source hydrodynamic code ATHENA++, for which we develop a method to calculate self-gravity for axially symmetric density distributions. For a fixed model of the wind injection, we explore the explosion characteristics for progenitors with zero-age main-sequence masses from 9 to 40 $\mathrm{M}_\odot$ and different degrees of rotation. Our outcomes reveal a wide range of explosion energies with $E_{\rm expl}$ spanning from $\sim 0.3 \times 10^{51}$ to $> 8 \times 10^{51}$ erg and ejecta mass $M_{\rm ej}$ from ~ 0.6 to $> 10\,\mathrm{M}_\odot$. Our results are in agreement with some range of the observational data of stripped-envelope and high-energy SNe such as broad-lined type Ic SNe, but we measure a stronger correlation between $E_{\rm expl}$ and $M_{\rm ej}$. We also provide an estimate of the ^{56}Ni mass produced in our models which goes from ~ 0.04 to $\sim 1.3\,\mathrm{M}_\odot$. The ^{56}Ni mass shows a correlation with the mass and the angular velocity of the progenitor: more massive and faster rotating progenitors tend to produce a higher amount of ^{56}Ni. Finally, we present a criterion that allows the selection of a potential collapsar progenitor from the observed explosion energy.

Key words: accretion, accretion discs – hydrodynamics – nuclear reactions, nucleosynthesis, abundances – supernovae: general.

1 INTRODUCTION

Massive stars ($\gtrsim 9\,\mathrm{M}_\odot$), at the end of their hydrostatic life, are expected to form an iron core and subsequently undergo a gravitational collapse. This core collapse marks the start of a complex sequence of events with various outcomes. The post-collapse evolution and final remnant properties depend on factors like the progenitor mass, its angular momentum, and magnetic field (e.g. Woosley 2010; Janka et al. 2012; Ugliano et al. 2012). Typically, stars with moderate mass tend to successfully explode through the heating by neutrinos emitted from the proto-neutron star (PNS), determining a classical core-collapse supernova (CCSN; e.g. Janka, Melson & Summa 2016; Mezzacappa 2020; Bollig et al. 2021; Burrows & Vartanyan 2021; Kuroda et al. 2022; Vartanyan, Coleman & Burrows 2022; Wang et al. 2022; Bruenn et al. 2023; Rahman et al. 2023 on the latest progress), while progenitors with an even higher zero-age main-sequence mass, $M_{\rm ZAMS} \gtrsim 16\,\mathrm{M}_\odot$ are more prone to fail the explosion (as indicated by Woosley & Heger 2006). The massive stars that fail to launch a successful explosion during the PNS phase collapse into a black hole (BH).

In the presence of an appreciable rotation of the progenitor stars, the BH should be subsequently surrounded by an accreting disc (see e.g. Woosley & Heger 2006). It has been shown that in failed SNe the wind created by the viscous heating inside the accretion disc may be a natural source of the SN energy with an explosion energy $E_{\rm expl} \gtrsim 10^{52}$ erg (MacFadyen & Woosley 1999; Popham, Woosley & Fryer 1999; Kohri, Narayan & Piran 2005) and it has been found to be rich in ^{56}Ni ($\geq 0.1\,\mathrm{M}_\odot$) (as shown by Just et al. 2022; Fujibayashi et al. 2024; Dean & Fernández 2024a). The activity of the disc surrounding the newly born BH can then also be a source of relativistic jets that account for gamma-ray bursts (GRBs). The BH-disc system is thus a promising engine to explain energetic supernovae such as broad-lined type Ic SNe (Type Ic-BL SNe or hypernovae) and their associated GRBs, as shown by observational studies such as Galama et al. (1998), Stanek et al. (2003), Campana et al. (2006), Xu et al. (2013; for a review, see also Woosley & Bloom 2006; Kumar & Zhang 2015). This scenario is known as *collapsar scenario*.

Considering the alternative case of a successful explosion, Obergaulinger & Aloy (2020) found that PNS with a mass ranging from 1.2 to 2.5 $\mathrm{M}_\odot$ can successfully launch explosions through either the

★ E-mail: ludovica.crosatomenegazzi@aei.mpg.de

neutrino-driven mechanism or the magnetohydrodynamics (MHD)-driven mechanism. A MHD-driven CCSN could occur when a strong magnetic field is associated with rapid rotation in the stellar core, and is a possible mechanism for the creation of magnetars. The MHD-driven CCSN scenario (also known as *proto-magnetar* scenario) presents a potential explanation for the GRBs and associated Type Ic-BL SNe (see e.g. Usov 1992; Metzger et al. 2011). In this scenario, rotation leads to global asymmetries of the shock wave, which translates into the formation of highly collimated, mildly relativistic bipolar outflow as shown by Burrows et al. (2007), Mösta et al. (2015), Bugli et al. (2019), Obergaulinger & Aloy (2020), Kuroda et al. (2020) in their MHD simulations. Grimmett et al. (2021) used hydrodynamics simulations based on this scenario to study the production of ^{56}Ni. In their most energetic models, where they observed an explosion energy $> 10^{52}$ erg, a significant amount of ejected ^{56}Ni was found, i.e. > 0.05–$0.45\,M_\odot$. These findings are consistent with values deduced from the light curves of Type Ic-BL SNe, which range from 0.12–0.8 $M_\odot$, with a median at $\sim$0.28 $M_\odot$, as determined by Taddia et al. (2019). Therefore, both the *collapsar* and *MHD-driven CCSN* scenarios are the currently favoured scenarios for the formation of GRBs and associated Type Ic-BL SNe. Historically, scenarios based on neutrino pair annihilation have been discussed through the years (see Woosley 1993; Piran 2004, for reviews), but they appear to be less efficient.

This paper is the extension of the previous work we presented in Menegazzi et al. (2024) (hereafter mentioned as Paper I). In the first study, we explored the properties of sub-relativistic outflow in the collapsar scenario, with the explosion fueled by a BH-accretion disc system. We performed two-dimensional axisymmetric hydrodynamics simulations for modelling the ejecta produced by the collapse of the massive, rotating star with $M_{\rm ZAMS} = 20\,M_\odot$ taken from Aguilera-Dena et al. (2020). Then, by varying the parameters of the injected wind, we investigated their effect on the ejecta properties such as mass, velocity, geometry, and ^{56}Ni production.

For this progenitor, our analysis unveiled a vast range of explosion energies with $E_{\rm expl}$ spanning from very low energy $\sim 5 \times 10^{49}$ erg to Ic-BL SN energy ($\sim 3 \times 10^{52}$ erg). This distinction depends on whether the ram pressure of the injected matter is stronger than that of the infalling envelope, effectively pushing the stellar envelope outward or not. Our results in Paper I showed that the explosion energies we measured were in good agreement with observational data for stripped-envelope SNe presented by Taddia et al. (2019) and Gomez et al. (2022) confirming that the disc wind generated from the BH-disc system in a failed SN may naturally be a source of the SN energy as suggested in previous studies by Woosley (1993), MacFadyen & Woosley (1999), Popham et al. (1999). Because of these results, we decided to further investigate the variety of the explosion properties using the same scenario as in Paper I, but expanding the parameter space by varying the mass and the initial rotational velocity of the progenitor. In this study, we fix the parameter of the injected wind while varying the progenitor structure (a detailed description of the choice of the parameters is presented in Section 2). We employ a range of different progenitors with the same composition dominated by oxygen outside the iron core (see Woosley & Heger 2006; Aguilera-Dena et al. 2020). Then, we sample them with respect to their $M_{\rm ZAMS}$ and vary their degree of rotation, while holding the wind parameters the same.

Our hydrodynamics model based on the collapsar scenario is inspired by those used in fully general relativistic hydrodynamics simulations (Fujibayashi et al. 2024), which we here simplified. None the less, we will show that this simplified method can reproduce the overall feature of the more detailed simulations, and hence, it is useful for the interpretation of the observational data.

This paper is organized as follows. In Section 2, we first briefly summarize our hydrodynamics code that has been outlined in Paper I and we also use for this work, and then we describe the physics of the progenitor stars we employ (taken from Woosley & Heger 2006; Aguilera-Dena et al. 2020) and the added parameter for the magnitude of the angular velocity. We present our results in Section 3, where we focus especially on the variety of the explosion energy and the ^{56}Ni production and study their dependence on the variation of the initial parameters and progenitor models. In this section, we also compare our results with observational data. Then, Section 4 contains a discussion about the implication of our results, also considering those obtained in Paper I and their observational counterpart. Finally, we summarize this work in Section 5. The Appendixes provide an insight into the hydrodynamical evolution of some models excluded from the analysis and an additional study of the effect of the wind injection model on the explosion of the 35 $M_\odot$ progenitor of Aguilera-Dena et al. (2020). Throughout this paper, G denotes the gravitational constant.

2 METHOD AND PARAMETERS

In this work, we numerically explore the collapsar scenario. Specifically, we focus on massive, fast-rotating stars in which the neutrino-driven explosion during the PNS phase does not take place, causing the PNS to collapse into a BH (failed CCSN). We model the explosion of a compact progenitor star post the BH formation. We perform two-dimensional (axisymmetric) Newtonian simulations using the open-source multidimensional hydrodynamics code ATHENA++ (Stone et al. 2020) to which we added the self-gravity by solving the Poisson's equation under the axial symmetry (the implementation is presented in Paper I). Additionally, in our simulations, we model the central engine in a semi-analytical way by evolving the BH and the disc through the transfer of matter and angular momentum. This method follows the prescriptions given by Kumar, Narayan & Johnson (2008) on which we add the contribution of the disc as described by Hayakawa & Maeda (2018).

The thermodynamical history of the ejecta is obtained using tracer particles in the method provided in Paper I. This method allows us to follow the evolution of the tracer particles backward in time and also to distinguish the fluid elements of the injected matter (coming from the inner boundary) from those originating from the stellar envelope (for a detailed description, see Paper I). If the maximum temperature of a tracer particle is higher than the critical temperature 5 GK for nuclear statistical equilibrium (e.g. Woosley, Heger & Weaver 2002), we assume that ^{56}Ni is synthesized with mass assigned to the tracer particle. As for the injected matter, since it lacks the thermodynamical history, we estimate the mass of ^{56}Ni by evaluating the temperature of the disc when the matter is injected. We, then, measure the ratio between the injected matter experiencing temperature higher than 5 GK and the total injected mass, and multiply it to the injected mass to get the amount of ^{56}Ni produced in this component of the ejecta. The method used to estimate the temperature of the injected matter is presented in Appendix B. As we will see in Section 3, we estimate that 40–60 per cent of the injected mass becomes ^{56}Ni with our procedure. We do not perform a full nucleosynthesis calculation and use the critical temperature 5 GK to approximately estimate the ^{56}Ni mass produced in the ejecta because of the lack of knowledge about the injected matter and the fact that it dominates over the mass originating from the stellar envelope (see Section 3.4).

It is worth reminding that in this work, we assume that the entire stellar component of the injected matter experiencing $T > 5$ GK becomes ^{56}Ni. This may be a reasonable assumption considering recent global viscous hydrodynamic studies in the collapsar scenario, in which they find an ejecta Y_e distribution that narrowly peaks around $Y_e \sim 0.5$ (Just et al. 2022; Dean & Fernández 2024a,b; Fujibayashi et al. 2024). However, some studies showed that collapsar discs may become neutron-rich (Siegel, Barnes & Metzger 2019; Miller et al. 2020), and more recently the first 3D neutrino-transport general-relativistic magnetohydrodynamic (νGRMHD) collapsar simulations performed by Issa et al. (2024) found the conditions for the development of neutron-rich ejecta in such scenario (measuring $Y_e \lesssim 0.3$). If the ejecta electron fraction is lower (i.e. $Y_e < 0.5$), the estimates of the ^{56}Ni would be different. In such a scenario, the main product of the nucleosynthesis is not expected to be ^{56}Ni, but rather heavier nuclei (Siegel et al. 2019). As a result, the mass fraction of ^{56}Ni of the injected matter would be substantially smaller than those estimated with the procedure used in this work.

2.1 Computational set-up

In this work, all simulations are performed on an axisymmetric grid using spherical-polar coordinates. The polar angle of our domain spans from 0 to π with 128 grid points uniformly distributed, leading to a zone width of $\Delta\theta = 0.0245$ rad. The radial dimension ranges from 10^8 cm ($r_{\rm in}$) to 3.3×10^{10} cm ($r_{\rm out}$) and it is divided into 220 zones. The grid zone size Δr is obtained by increasing the mesh size with a constant factor $\Delta r_i = \alpha \Delta r_{i-1}$ where $\alpha \approx 1.03$ ensures an approximately squared shape for all zones (i.e. $\Delta r_i \approx r_i \Delta\theta$; for more details see Paper I).

The inner radius $r_{\rm in}$ determines the inner boundary of the computational domain, and it is the same through all simulations. This cut is done to exclude the central engine from the computational domain and consider it embedded in the central part of the star. By this cut, computational costs are significantly saved, as evolving the central engine semi-analytically rather than numerically significantly reduces the simulation time.

Instead of solving the hydrodynamics inside $r_{\rm in}$, we evolve the BH and disc assumed to be embedded there. Specifically, their masses ($M_{\rm BH}$ and $M_{\rm disc}$) and angular momenta ($J_{\rm BH}$ and $J_{\rm disc}$) are evolved according to the mass and angular momentum fluxes at $r_{\rm in}$ (see Paper I for details). The initially enclosed mass and angular momentum inside $r_{\rm in}$ are assumed to be those of the initial mass of the BH (see Section 2.3). The outer radius, which is located outside the stellar surface of our progenitor models, is also kept fixed for all simulations.

2.2 The equation of state

The thermodynamical properties of the star are described by the same equation of state (EOS) as employed in Paper I which includes ions, radiation, electrons, and e^-–e^+ pair (we also refer to the EOS described in Timmes & Swesty 2000 and Takahashi et al. 2016). In this work, we suppose that oxygen is the only component for the ion (i.e. $Y_e = 0.5$), resulting in a ^{16}O mass fraction of 1. This decision was made considering the composition of our progenitor model, which is dominated by oxygen outside the iron core (see Aguilera-Dena et al. 2020).

2.3 Inner boundary condition and parameters

The model used in this work is the same as in Paper I, which is based on the collapsar disc wind scenario and inspired by Fujibayashi et al.

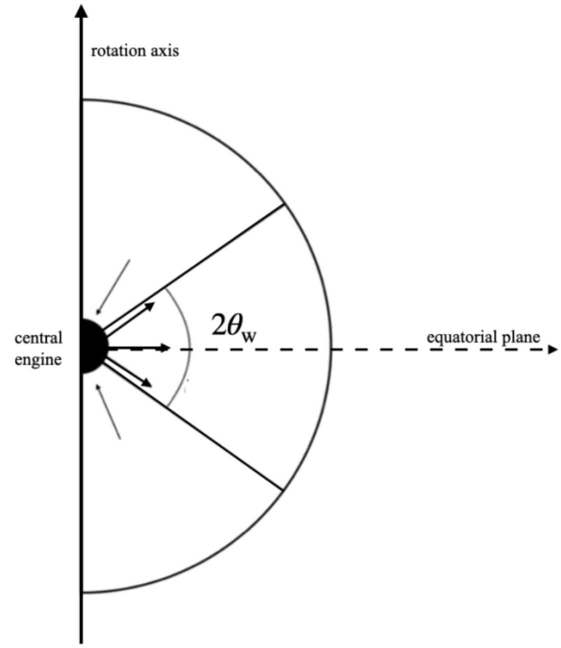

Figure 1. Schematic picture of the explosion in the collapsar scenario. $2\theta_w$ represents the angle for which we allow the wind outflow. Outside this angle, the matter is only allowed to infall towards the central engine. The figure also shows the rotation axis and the equatorial plane.

(2024; see also Just et al. 2022 and Dean & Fernández 2024a). We set the inner boundary conditions so that the wind is launched after the disc formation toward the non-axis direction (see section 2.6 of Paper I for a detailed description of the inner boundary conditions). In the early stages, before the disc formation, we allow material to flow toward the central engine for $r < r_{\rm in}$ (outflow condition). After the disc formation ($M_{\rm disc} > 0$), we set the wind injection from the inner boundary within a half opening angle of $\theta_w = \pi/4$ directed along the equatorial plane. Outside the injection angle, we inhibit matter flowing from the central engine into the computational domain by setting zero fluxes (reflecting boundary condition) when the radial velocity in the first active cell is positive while letting the mass infall to the central engine if it is negative. The geometry employed in our simulations is illustrated in Fig. 1.

The choice of setting the half opening angle as $\theta_w = \pi/4$ and directing it along the equatorial plane was made considering the results of global simulations obtained by Fujibayashi et al. (2024), Just et al. (2022), and Dean & Fernández (2024a). Their simulations, indeed, show that the wind matter remains confined (focused, collimated) within an opening angle of roughly $\pi/2$ along the equatorial plane (see fig. 2 in Fujibayashi et al. 2024, figs 3 and 4 in Just et al. 2022, or fig. 3 in Dean & Fernández 2024a for reference). Additionally, the outflow we study in this work is non-relativistic, leading the explosion configuration to rapidly become spherical; hence the θ_w is unlikely to significantly change the global result (an analysis of the effect of the opening angle on the outflow properties is presented in Appendix A). Considering these findings, we then use $\theta_w = \pi/4$ as fiducial value.

We set the wind density ρ_w using a parabolic density profile described in Paper I. The total specific energy of the disc wind at the inner boundary is assumed to be a fraction of the specific kinetic energy with the disc escape velocity $v_{\rm esc}$ as:

$$\frac{1}{2}v_w^2 + f_{\rm therm}\frac{1}{2}v_w^2 + \Phi = \xi^2 \frac{1}{2} v_{\rm esc}^2\,, \tag{1}$$

where $v_{\rm esc} := \sqrt{2GM_{\rm BH}/r_{\rm disc}}$ with $r_{\rm disc} := j_{\rm disc}^2/GM_{\rm BH}$ and $j_{\rm disc} := J_{\rm disc}/M_{\rm disc}$. In equation (1), Φ is the gravitational potential which satisfies the Poisson's equation:

$$\Delta\Phi = 4\pi G\rho\,, \tag{2}$$

where ρ is the mass density of the fluid, and the specific internal energy of the wind, $e_{\rm int,w}/\rho_{\rm w} = (1/2) f_{\rm therm} v_{\rm w}^2$, is defined as a fraction of the wind kinetic energy through the free parameter $f_{\rm therm}$. The fudge factor ξ denotes the uncertainties due to incomplete knowledge of the disc structure (Hayakawa & Maeda 2018). The outflow pressure is calculated from the EOS with the density ($\rho_{\rm w}$) and internal energy ($e_{\rm int,w}$) as input parameters.

Equation (1) indicates that if the total specific energy $(1/2)v^2 + e_{\rm int}/\rho + \Phi$ is conserved, the asymptotic velocity of the injected matter is $\xi v_{\rm esc}$.

Part of the injected matter could fall back to the centre when it has a ram pressure smaller than that of the infalling envelope. If this happens and the injected matter that is pushed back has $j > j_{\rm ISCO}$ where $j_{\rm ISCO}$ is the specific angular momentum at the innermost stable circular orbit (ISCO; Bardeen, Press & Teukolsky 1972), it would become part of $M_{\rm disc}$ again and hence re-injected into the computational domain. To avoid the recycling of the injected matter, as we did in Paper I, we do not allow the injected matter to fall back to the disc, but only to the BH by setting the angular momentum of the injected matter to zero.

In this work, we fix the parameters of the wind following the results obtained in our previous work. The wind parameters are the wind time-scale $t_{\rm w}$, the accretion time-scale $t_{\rm acc}$, the ratio between the radial velocity of the outflow and the escape velocity ξ, and $f_{\rm therm}$ (see equation 1). This regulates the rate at which material is accreted on to the BH from the disc, and hence aids in monitoring the central engine's dynamics (see Kumar et al. 2008 for more details).

Our aim of the present study is to reproduce a highly energetic explosion with a large production of ^{56}Ni, comparable to observed high-energy SNe. Therefore, referring to fig. 7 of Paper I, all simulations in this work are performed setting a wind time-scale $t_{\rm w} = 3.16$ s, the accretion time-scale $t_{\rm acc} = 10$ s, the factor $\xi^2 = 0.1$ and $f_{\rm therm} = 0.1$ (but see Appendix D for a complementary study). These parameters characterized the model M20_3.16_3.16_0.1_0.10 of Paper I, which undergoes an energetic explosion with $E_{\rm expl} = 3.0 \times 10^{51}$ erg and has the ejecta mass of $M_{\rm ej} = 3.4\,{\rm M}_\odot$, which is also in good agreement with the results obtained by Fujibayashi et al. (2023) for the same progenitor.[1]

2.4 Diagnostics

In this subsection, we outline the approach used to calculate the properties of the ejecta and injected matter. We define ejecta mass $M_{\rm ej}$ as the sum of unbound matter mass. The explosion energy $E_{\rm expl}$ is the energy carried by the unbound matter. The unbound matter is evaluated through the Bernoulli criterion, which takes into account the thermal effect on the matter and the effects of the gravitational potential, and is defined as:

$$B := \frac{e_{\rm t} + P}{\rho} + \Phi > 0, \tag{3}$$

[1]Fujibayashi et al. (2023) measured the ejecta mass of $M_{\rm ej} = 2.2\,{\rm M}_\odot$ and an explosion energy of $E_{\rm expl} = 2.2 \times 10^{51}$ erg at the end of their simulation. These values are lower than ours, but they should be considered as the lower limits since they were still growing at the end of their simulation; in a longer term simulation, these values can be larger.

where $e_{\rm t} = e_{\rm int} + e_{\rm kin}$ is the sum of the internal ($e_{\rm int}$) and kinetic ($e_{\rm kin} = \rho v^2/2$) energy densities, and P is the pressure of the fluid, respectively.

Using the Bernoulli criterion, we track the evolution of the ejecta mass and energy at every time-step by integrating the equations:

$$M_{\rm ej} = {\rm r}_{\rm out}^2 \int_0^t \int_{B>0, v_r>0} \rho v_r {\rm d}S{\rm d}t + \int_{B>0, v_{\rm r}>0} \rho {\rm d}^3x, \tag{4}$$

$$E_{\rm expl} = {\rm r}_{\rm out}^2 \int_0^t \int_{B>0, v_{\rm r}>0} \rho B v_{\rm r} {\rm d}S{\rm d}t + \int_{B>0, v_{\rm r}>0} (e_{\rm t} + \rho\Phi) {\rm d}^3x, \tag{5}$$

where, dS denotes the surface integral element. The injected mass $M_{\rm inj}$ represents the matter coming from the central engine with a positive mass flux at the inner boundary $r_{\rm in}$. It is defined as:

$$M_{\rm inj} = r_{\rm in}^2 \int_0^t \int_{v_{\rm r}>0} \rho v_{\rm r} {\rm d}S{\rm d}t. \tag{6}$$

We consider the injected energy $E_{\rm inj}$ as the energy carried by $M_{\rm inj}$ with positive binding energy. We, then, compute the injected energy $E_{\rm inj}$ applying the Bernoulli criterion as follows:

$$E_{\rm inj} = r_{\rm in}^2 \int_0^t \int_{v_{\rm r}>0} \rho B v_{\rm r} {\rm d}S{\rm d}t. \tag{7}$$

The Bernoulli criterion allows us also to evaluate the energy of the bounded matter (i.e. the binding energy) at the beginning of the injection which we define as:

$$E_{\rm bind,inj} = \int_{B<0, v_{\rm r}<0} (e_{\rm t} + \rho\Phi) {\rm d}^3x. \tag{8}$$

2.5 Progenitor parameters

Progenitors of long GRBs have been suggested to be rapidly rotating, rotationally mixed massive stars. Therefore, based on our aforementioned aim of investigating the effect of the progenitor structure on the explosion properties, in this work, we fix the parameters of the wind injection (explained in Section 2.3) while changing the progenitor models. We, then, select some massive, rapidly rotating, rotationally mixed stars from the stellar evolution models of Aguilera-Dena et al. (2020) (throughout this paper we will refer to the $M_{\rm ZAMS}$ of the model also as $M_{\rm prog}$). In particular, we choose nine stars with $M_{\rm ZAMS} = 9, 15, 17, 20,$[2] $22, 25, 30, 35,$ and $40\,{\rm M}_\odot$. For each of them we, then, consider five different degrees of rotation, the original rotational profile of the progenitor Ω_0 (as given by Aguilera-Dena et al. 2020) and four more for which the angular velocity is modified from the original one Ω_0. These are obtained multiplying Ω_0 by $n_\Omega = 0.5,\ 0.6,\ 0.8,$ and 1.2 following Fujibayashi et al. (2024).

In order to further investigate the dependence of the ejecta mass, the explosion energy, and the ^{56}Ni production on the progenitor structure, we also perform additional simulations using models with different characteristics. Specifically, we employ the progenitor models `16TI` and `35OC` from Woosley & Heger (2006) with no modification of the angular velocity. These stars have a larger angular momentum in an inner region than those of Aguilera-Dena et al. (2020) at the onset of the stellar collapse.

Considering the progenitor stars of Aguilera-Dena et al. (2020), in our model selection, we include both progenitors that are expected to undergo a successful explosion during the PNS phase and progenitors that are expected to fail the explosion and lead to the BH formation, according to the core-compactness criterion (Ertl et al. 2016 and Müller et al. 2016: The progenitors' core-compactness parameter is presented in fig. 4 in Aguilera-Dena et al. 2020). This choice is

[2]This is the same progenitor used in Paper I.

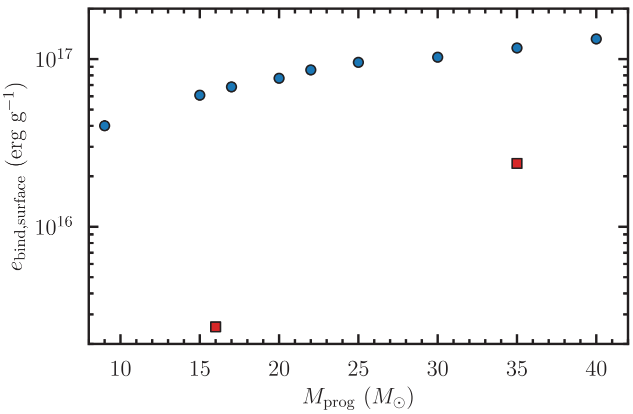

Figure 2. The specific gravitational binding energy at the surface of the progenitor star $e_{\rm bind,surface}$ as a function of the progenitor mass $M_{\rm prog}$. $e_{\rm bind,surface}$ gives an estimate of the compactness of the entire star. The blue circles show $e_{\rm bind,surface}$ for the models of Aguilera-Dena et al. (2020), while the red squares indicate the results obtained using `16TI` and `35OC` (Woosley & Heger (2006).

made in order to cover a wide range of compactness of the *entire* star, which is likely to be relevant to the mass accretion rate after the disc formation (see Fujibayashi et al. 2024). For instance, higher compactness of the entire star leads to a higher mass accretion rate at a later stage of the collapse (i.e. after the disc formation), and Fujibayashi et al. (2024) showed that a higher mass-infall rate, typically from the carbon-oxygen layer of the star, amplifies the viscous and shock heating rates within the inner region of the disc, determining a large explosion energy. Therefore, studying different values of the entire star compactness allows us to investigate a large variety of mass accretion rates after the disc formation, which, in our scenario, may affect the outflow energy.

A measure of the compactness of the entire progenitor star can be given by estimating the specific gravitational binding energy at the surface of the star defined by:

$$e_{\rm bind,surface} = \frac{GM_*}{R_*}, \tag{9}$$

where M_* and R_* are the mass and the radius of the star, respectively. In Fig. 2, we show the value of $e_{\rm bind,surface}$ as a function of the progenitor mass for the models of Aguilera-Dena et al. (2020) (blue circles) and the `16TI` and `35OC` progenitors from Woosley & Heger (2006) (red squares). The figure shows that more massive stars have higher specific gravitational binding energy considering the models of Aguilera-Dena et al. (2020) because R_* depends only weakly on M_* for their models. By contrast, for the models of Woosley & Heger (2006), R_* is much larger than that for the models of Aguilera-Dena et al. (2020), and thus, the specific gravitational binding energy is much smaller. This suggests that the models of Woosley & Heger (2006) have the possibility of more energetic explosion.

3 RESULTS

In this section, we will first analyse the mechanism that drives the explosion in our models and will investigate the dependence of the explosions on the progenitor mass and angular velocity (Section 3.1). We also compare those to some observational data (Section 3.2). We then present a way to predict the explosion energy from our progenitor models (Section 3.3). Finally, we will show the effect of the progenitor mass $M_{\rm prog}$ and the magnitude of the angular velocity n_Ω on the final ^{56}Ni production (Section 3.4). The models studied in this work, with the most important properties of their ejecta and the results of the ^{56}Ni production, are summarized in Table 1.

In the final analysis of the results, some models were excluded due to their physical inconsistency. The inconsistency arises from the fact that in these models, the accretion disc grows in the computational domain of $r_{\rm in} \le r \le r_{\rm out}$. In our numerical modelling there are no processes that launch the wind from the disc in the computational domain. Consequently, the injected mass and energy are not correctly assessed for such models. On the other hand, for the other models, the mass and energy injection sets in before the disc is formed in the computational domain, and thus the result is considered to be physically consistent. Models showing the inconsistent behaviour are therefore excluded from the general analysis of the results presented here but are described in Appendix C and listed in Table C1.

3.1 Parameter dependence of the dynamics

To investigate the dependence of the explosion properties on the progenitor models, we fixed the wind parameter to be the same for all simulations. As explained in Section 2.3, we employed the wind parameter of the model M20_3.16_3.16_0.1_0.10 from Paper I (i.e. $t_{\rm w} = 3.16$ s, $t_{\rm acc}/t_{\rm w} = 3.16$, $\xi^2 = 0.1$, and $f_{\rm therm} = 0.1$) because it undergoes an energetic explosion with explosion energy and ^{56}Ni mass comparable to those measured in energetic SNe.

In the left panel of Fig. 3, we compare the disc formation time $t_{\rm df}$, at which $M_{\rm disc}$ becomes non-zero, with the injection time $t_{\rm inj}$ (the time at which the mass and energy fluxes at the inner boundary become positive and the matter unbound) for a sample of progenitors (among those taken from Aguilera-Dena et al. 2020) with four different rotational levels.

Both panels of Fig. 3 show a correlation between the disc formation time and the progenitor structure, specifically, the magnitude of the angular velocity: $t_{\rm df}$ is longer for progenitors with lower values of n_Ω. It is possible to explain this behaviour considering that in slower rotating models the matter that has a sufficient angular momentum to form the disc is located at larger radii, thus taking longer time to fall into the central region and form the disc.

To prove the above speculation, we evaluate the free-fall time of the mass shell that has a specific angular momentum sufficiently large to form the disc, which may give an approximate estimation of $t_{\rm df}$. We here assume that during the formation and the growth of a BH, the specific angular momentum is conserved. Under this assumption and considering that the region with the enclosed mass $M_{\rm encl}$ collapses to the BH without forming a disc, it is possible to estimate the mass and angular momentum of the formed BH for a given profile of the specific angular momentum as a function of the enclosed mass, $j(M_{\rm encl})$ (Shibata & Shapiro 2002; Shibata 2003), defined as

$$j = \frac{1}{4\pi r^2}\int_0^{2\pi}\int_0^{\pi} \Omega(r) r^4 \sin^3\theta {\rm d}\theta {\rm d}\phi = \frac{2}{3} r^2 \Omega(r). \tag{10}$$

Here, $\Omega(r)$ is the angular velocity profile as a function of the spherical radius only, which is assumed in stellar evolution calculations (Zahn 1992). Both j and $M_{\rm encl}$ are functions of r.

In Fig. 4, we show the average specific angular momentum of a mass shell, $(2/3)r^2\Omega$, as a function of $M_{\rm encl}$ for the model of $M_{\rm prog} = 20\,{\rm M}_\odot$ with different degrees of rotation: $n_\Omega = 0.5$, 0.6, 0.8, 1.0 and 1.2 (solid lines, where the colour distinguishes n_Ω). We also plot $j_{\rm ISCO}$ for a BH that has mass $M_{\rm encl}$ and angular momentum $J_{\rm encl}$ for each model (dashed lines), and we highlight with filled circles the points at which $j = j_{\rm ISCO}$ before getting larger. We refer to the mass when $j = j_{\rm ISCO}$ as $M_{\rm encl}^{\rm df}$. When the mass shell falls into the centre, a

Table 1. Model description and key results. The model's name contains information about the progenitor mass and the magnitude of the angular velocity: the first number corresponds to $M_{\rm prog}$ and the second indicates the factor by which the original degree of rotation has been multiplied. From left to right, the columns list the cumulative injected energy, ejecta mass, explosion energy, average ejecta velocity, the number of tracer particles located within the ejecta, the mass of ejecta component originating from the injected matter, the ratio between the injected matter that is estimated to experience temperature higher than 5 GK and the total injected mass, the mass of ejecta component that is originated from the computational domain and experiences temperature higher than 5 GK, along with the number of tracer particles in parenthesis, the total mass of the ejecta which experiences temperature higher than 5 GK.

Model	$E_{\rm inj}$ (10^{51} erg)	$M_{\rm ej}$ ($\mathrm{M}_\odot$)	$E_{\rm expl}$ (10^{51} erg)	$v_{\rm ej}$ (10^3 km s^{-1})	$N_{\rm p}$	$M^{\rm inj}_{\rm ej}$ ($\mathrm{M}_\odot$)	$M^{\rm inj}_{>5\,\rm GK}/M^{\rm inj}$	$M^{\rm stellar}_{\rm ej,>5\,GK}$ ($N^{\rm stellar}_{\rm ej,>5\,GK}$) ($\mathrm{M}_\odot$)	$M_{\rm ej,>5\,GK}$ ($\mathrm{M}_\odot$)
AD009x0.5	0.59	0.56	0.26	6.67	38681	0.19	0.39	0.00 (0)	0.07
AD015x0.5	2.51	1.49	0.93	7.79	4269	0.46	0.44	0.01 (160)	0.21
AD017x0.5	2.81	1.52	0.91	7.61	43049	0.53	0.44	0.01 (111)	0.24
AD020x0.5	3.37	1.36	0.86	7.82	37600	0.51	0.46	0.01 (145)	0.24
AD009x0.6	0.93	0.78	0.35	6.72	52445	0.10	0.43	0.00 (1)	0.04
AD015x0.6	3.15	1.88	1.34	8.32	41193	0.64	0.48	0.02 (187)	0.33
AD017x0.6	3.63	1.94	1.43	8.46	43309	0.65	0.48	0.017 (211)	0.33
AD020x0.6	4.67	1.77	1.35	8.61	39282	0.50	0.50	0.01 (165)	0.26
AD022x0.6	5.80	2.00	1.95	9.74	61595	0.75	0.52	0.01 (123)	0.40
AD025x0.6	6.22	1.85	1.60	9.17	43669	0.54	0.54	0.02 (249)	0.31
AD009x0.8	1.58	1.12	0.78	8.24	59195	0.20	0.54	<0.01 (12)	0.12
AD015x0.8	3.82	2.43	1.61	8.01	39308	0.78	0.44	0.02 (208)	0.36
AD017x0.8	4.71	2.50	2.04	8.91	45816	0.83	0.52	0.04 (353)	0.47
AD020x0.8	6.45	2.28	1.98	9.20	42409	0.54	0.50	0.03 (277)	0.30
AD022x0.8	7.91	3.03	3.36	10.39	43355	1.20	0.55	0.02 (136)	0.68
AD025x0.8	9.77	2.82	3.13	10.63	89755	0.88	0.64	0.02 (138)	0.58
AD035x0.8	11.87	2.80	2.86	9.97	64595	1.11	0.55	<0.01 (24)	0.62
AD009x1.0	2.03	1.39	1.11	8.82	45629	0.32	0.64	<0.01 (8)	0.21
AD015x1.0	4.21	2.37	1.37	7.50	41690	0.53	0.45	0.02 (170)	0.26
AD017x1.0	5.21	3.07	2.21	8.36	40497	1.09	0.48	0.05 (344)	0.57
AD020x1.0	7.10	3.33	3.04	9.42	45856	1.23	0.52	0.06 (380)	0.70
AD022x1.0	9.05	3.61	3.97	10.28	49035	1.44	0.56	0.04 (278)	0.85
AD025x1.0	11.50	3.94	4.75	10.82	49748	1.52	0.59	0.05 (257)	0.95
AD030x1.0	13.46	4.40	5.16	10.68	55761	1.88	0.54	0.02 (57)	1.04
AD035x1.0	16.20	4.30	5.15	10.80	53789	1.70	0.56	<0.01 (28)	0.96
AD040x1.0	17.55	3.73	3.38	9.37	38332	1.36	0.57	0.10 (663)	0.88
AD009x1.2	2.38	1.56	1.35	9.16	45537	0.39	0.65	<0.01 (14)	0.26
AD015x1.2	4.19	2.98	1.74	7.52	62670	0.82	0.45	0.01 (83)	0.38
AD017x1.2	5.55	3.28	2.25	8.17	39335	1.07	0.49	0.04 (294)	0.56
AD020x1.2	7.83	3.75	3.46	9.45	61895	1.24	0.53	0.06 (378)	0.72
AD022x1.2	9.77	4.07	4.16	9.96	72141	1.49	0.56	0.08 (381)	0.91
AD025x1.2	13.38	4.74	5.70	10.81	65685	1.72	0.58	0.10 (445)	1.10
AD030x1.2	15.00	5.27	6.19	10.84	49952	1.98	0.56	0.093 (396)	1.20
AD035x1.2	19.73	5.58	7.98	11.79	46960	2.21	0.55	0.04 (172)	1.26
AD040x1.2	22.86	5.64	8.15	11.82	58541	2.28	0.55	0.017 (34)	1.27
16TI	3.28	5.32	1.20	4.76	87957	0.60	0.41	0.015 (1261)	0.26
35OC	14.42	10.67	5.18	6.99	145059	1.88	0.47	0.25 (11268)	1.14

disc is expected to be formed. This plot shows that a BH is likely to grow more before the disc formation for lower values of n_Ω, i.e. to $M^{\rm df}_{\rm encl} \approx 6.8, 7.8, 9.2, 10.1$ and $12.1\,\mathrm{M}_\odot$ for $n_\Omega = 1.2, 1.0, 0.8, 0.6$ and 0.5, respectively. This procedure of comparing the specific angular momentum with $j_{\rm ISCO}$ has applied to all the models to calculate the mass coordinate $M^{\rm df}_{\rm encl}$ and the corresponding radius $R^{\rm df}_{\rm encl}$. Fig. 5 shows the results of this calculation as a function of the progenitor mass for both $M^{\rm df}_{\rm encl}$ (upper panel) and $R^{\rm df}_{\rm encl}$ (lower panel). In this plot, we present results for a sample of the models taken from Aguilera-Dena et al. (2020) with $n_\Omega = 0.5, 0.6, 0.8, 1.0, 1.2$, and for the progenitor stars `16TI` and `35OC` (from Woosley & Heger (2006), right-pointing and left-pointing triangle respectively). The results presented in Figs 4 and 5 confirm our hypothesis that in progenitor stars with lower angular velocity, the matter with sufficiently high-angular momentum to form the disc is located at larger radii, hence presenting a longer disc formation time, $t_{\rm df}$.

We now calculate $t_{\rm ff}$ for the mass shell $M^{\rm df}_{\rm encl}$ as

$$t_{\rm ff} = \frac{\pi}{\sqrt{G M^{\rm df}_{\rm encl}}} \left(R^{\rm df}_{\rm encl}/2\right)^{3/2}. \quad (11)$$

In Fig. 6, we compare $t_{\rm ff}$ of the mass coordinate $M^{\rm df}_{\rm encl}$, at which the disc is expected to form (on the vertical axis), with $t_{\rm df}$ measured in the simulations (on the horizontal axis) for the same sample of progenitor models from Aguilera-Dena et al. (2020) used in Fig. 5 (i.e. the progenitor stars with $n_\Omega = 0.5, 0.8, 1.0$ and 1.2; $M_{\rm prog}$ is distinguished by colour while the marker indicates n_Ω) and the progenitor stars `16TI` and `35OC` (from Woosley & Heger 2006; right-pointing and left-pointing triangle, respectively). This plot clearly shows a linear correlation between the free-fall time analytically evaluated and the time at which the disc is formed in the simulations. It also confirms that the disc formation is supposed to take longer for slower rotating stars because $M^{\rm df}_{\rm encl}$ is located further

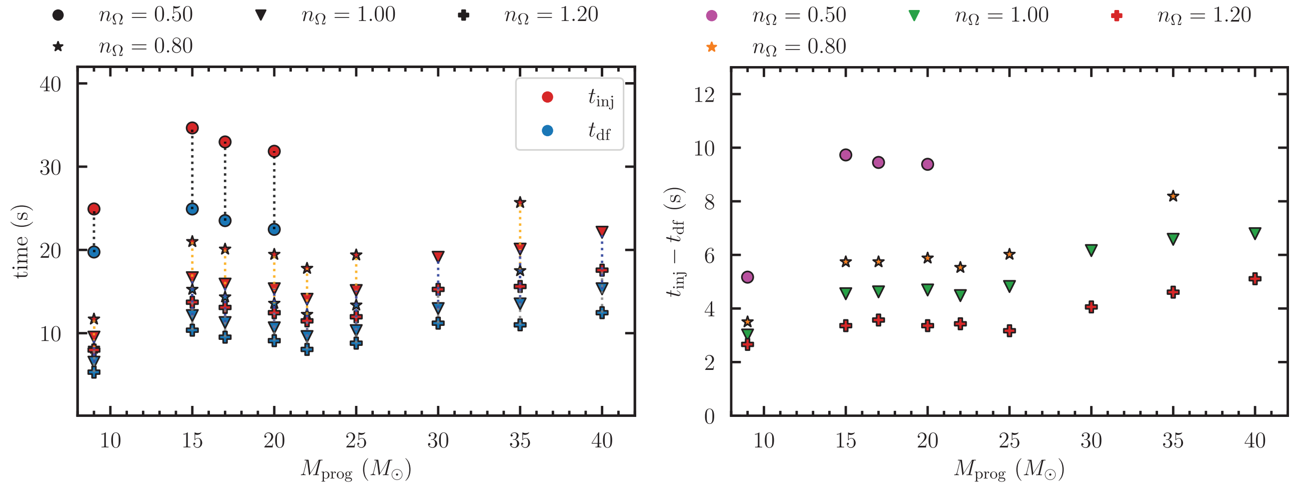

Figure 3. Left panel: disc formation time, $t_{\rm df}$ (blue dots), and injection time (red dots), $t_{\rm inj}$, as functions of the progenitor mass for a sample of models taken from Aguilera-Dena et al. (2020) with four degrees of rotation: $n_\Omega = 0.5$, 0.8, 1, and 1.2. Right panel: time difference between the disc formation and the beginning of the injection, $t_{\rm inj} - t_{\rm df}$ for the same four rotational levels. In this panel the colour and the shape distinguish the magnitude of the angular velocity.

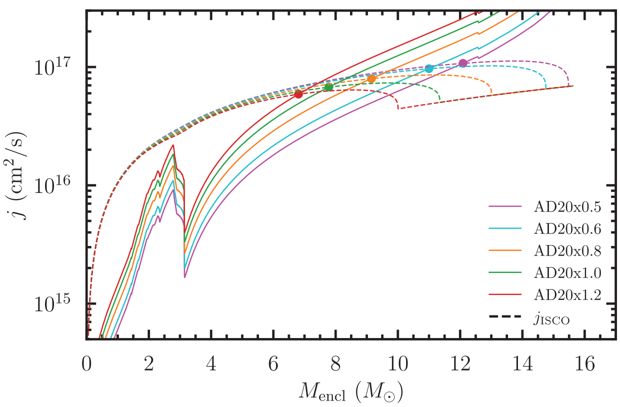

Figure 4. Specific angular momentum, j, as a function of the enclosed mass, $M_{\rm encl}$, for the model of $M_{\rm prog} = 20\,\mathrm{M}_\odot$ with different degrees of rotation: $n_\Omega = 0.5, 0.6, 0.8, 1.0$ and 1.2. The magnitude of the angular velocity is distinguished by the colour. We also plot $j_{\rm ISCO}$ for a given BH of mass $M_{\rm encl}$ and corresponding angular momentum $J(M_{\rm encl})$ by the dotted curves. The filled circles denote the points at which $j = j_{\rm ISCO}$ is satisfied for each progenitor model.

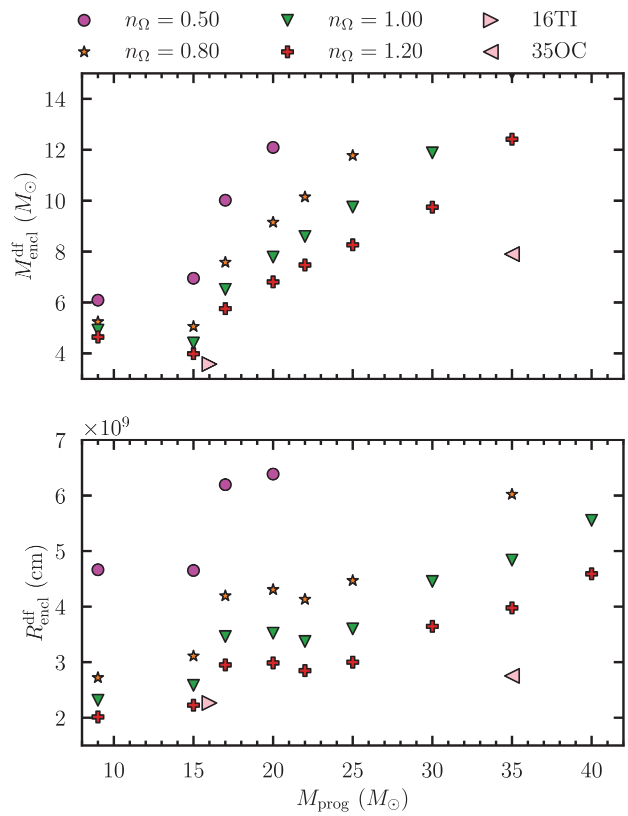

Figure 5. Upper panel: estimated BH mass at the disc formation $M^{\rm df}_{\rm encl}$ as a function fo the progenitor mass $M_{\rm prog}$. $M^{\rm df}_{\rm encl}$ is evaluated to be the enclosed mass of the progenitor with a specific angular momentum equal to $j_{\rm ISCO}$. Lower panel: The radius $R^{\rm df}_{\rm encl}$ of the mass coordinate $M^{\rm df}_{\rm encl}$ as a function of $M_{\rm prog}$. The results are shown for a sample of the progenitor models from Aguilera-Dena et al. (2020) with four degree of rotation $n_\Omega = 0.5, 0.8, 1.0, 1.2$ (results for progenitors with different magnitudes of the angular velocity is distinguished by different markers). We also show the results for the models `16TI` and `35OC` from Woosley & Heger (2006) (pink right-pointing and left-pointing arrow, respectively).

out in the envelope. Focusing on the specific values of $t_{\rm ff}$ and $t_{\rm df}$, we notice that in our simulations, the disc formation time is by a factor of $\approx$1.5 longer than the estimation with the free-fall time. This is likely due to the fact that the stellar envelope is not really free-falling due to the presence of the pressure in our simulations.

The disc formation is employed as the condition triggering the generation of the wind in our simulations. The injection of matter and energy through the inner boundary does not begin simultaneously with the wind formation, though, since the wind needs some time to induce a positive mass flux at the inner boundary and make the matter there unbound. This happens once the ram pressure of the injected matter wins over that of the infalling envelope, which is lower in the later times. Both panels of Fig. 3 show that, in our simulations, the time interval $t_{\rm inj} - t_{\rm df}$ varies from $\sim$2 s for $n_\Omega = 1.2$ to $\sim$10 s for $n_\Omega = 0.5$ and, for a fixed magnitude of the rotation, it remains mostly constant until $M_{\rm prog} \approx 25\,\mathrm{M}_\odot$ and tends to slightly increase

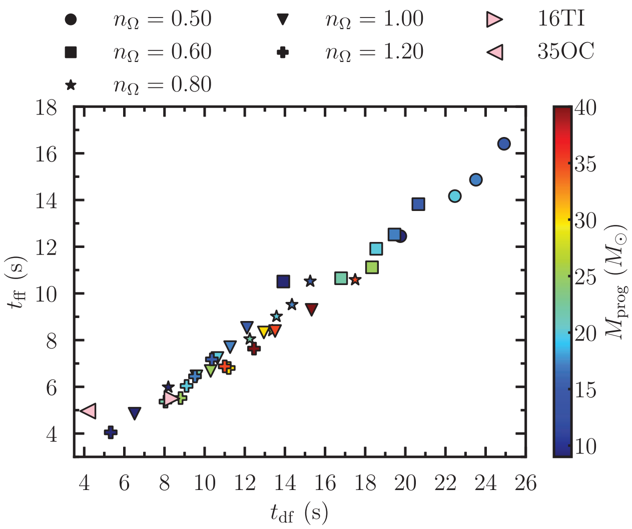

Figure 6. Estimated free-fall time $t_{\rm ff}$ of the enclosed mass at which the disc is formed against the disc formation time $t_{\rm df}$ for a sample of the progenitor models from Aguilera-Dena et al. (2020) with four degrees of rotation: $n_\Omega = 0.5, 0.8, 1.0, 1.2$. Results for progenitors with different magnitude of the angular velocity is distinguished by different markers, while the colour indicates the progenitor mass $M_{\rm prog}$. We also show the results for the models `16TI` and `35OC` from Woosley & Heger (2006) (pink right-pointing and left-pointing arrow, respectively).

for $M_{\rm prog} > 30\,{\rm M}_\odot$. This can be explained considering that the stellar radius of the progenitors depends only weakly on the progenitor mass for the stellar-evolution models of Aguilera-Dena et al. (2020). Thus, for larger values of $M_{\rm prog}$, the ram pressure of the infalling matter can be higher, dominating over that of the injected matter, for longer times. Eventually, in all simulations, the ram pressure of the injected matter becomes larger than that of the infalling envelope, driving the explosion.

We then discuss the explosion energy and ejecta mass. In Fig. 7, we present the results of all simulations in terms of the injected and explosion energy ($E_{\rm inj}$ and $E_{\rm exp}$). In the left panel, we plot the ratio of the explosion energy to the injection energy, $E_{\rm expl}/E_{\rm inj}$, for the models from Aguilera-Dena et al. (2020) with different values of n_Ω and from the models `16TI` and `35OC` as a function of $M_{\rm ej}$ and in the right panel, we display separately $E_{\rm inj}$ (open markers) and $E_{\rm expl}$ (filled markers) as functions of the ejecta mass. We also show the results of $E_{\rm expl}$ obtained in Paper I for the model AD020x1.0 with grey $\times$-markers.

The left panel of Fig. 7 shows that the explosion energy represents 20–60 per cent of the injected energy for our models. The conversion efficiency of $E_{\rm inj}$ into $E_{\rm expl}$ is below unity because part of the injected energy is used to overcome the binding energy of the infalling envelope and another fraction is pushed back to the centre by the infalling matter, preventing it to contribute to the ejecta. From this plot, it is also evident that progenitors with higher angular velocity have a larger ejecta mass, while the values of $M_{\rm prog}$ seem to affect the efficiency of $E_{\rm expl}/E_{\rm inj}$, i.e. for more massive progenitors the ratio $E_{\rm expl}/E_{\rm inj}$ tends to be smaller. This behaviour can be explained by considering that the more massive progenitors have more gravitational potential energy that the injected matter should overcome for the explosion (cf. Fig. 2).

The right panel of Fig. 7 shows that more massive progenitors have larger values of $E_{\rm expl}$ and $M_{\rm ej}$ (in the case of the progenitors of Aguilera-Dena et al. (2020), for a fixed value of n_Ω). Both $E_{\rm expl}$ and $E_{\rm inj}$ show a continuous distribution with respect to the ejecta mass. Considering the distributions of these quantities for the models of Aguilera-Dena et al. (2020), the explosion energy ranges from $E_{\rm expl} = 0.3 \times 10^{51}$ erg for a model with $M_{\rm prog} = 9\,{\rm M}_\odot$ and $n_\Omega = 0.5$ to $E_{\rm exp} = 8.2 \times 10^{51}$ erg for a model with $M_{\rm prog} = 40\,{\rm M}_\odot$ and $n_\Omega = 1.2$ and the injected energy from $E_{\rm inj} = 0.6 \times 10^{51}$ erg to $E_{\rm inj} = 2.3 \times 10^{52}$ erg for the same two models. The only point slightly detached from the rest of the distribution are those of the $9\,{\rm M}_\odot$ progenitor with $n_\Omega = 0.5$ (AD009x0.5) and $n_\Omega = 0.6$ (AD009x0.6). None the less, the explosion energy follows the global trend even for these simulations. Therefore it is reasonable to assume that the

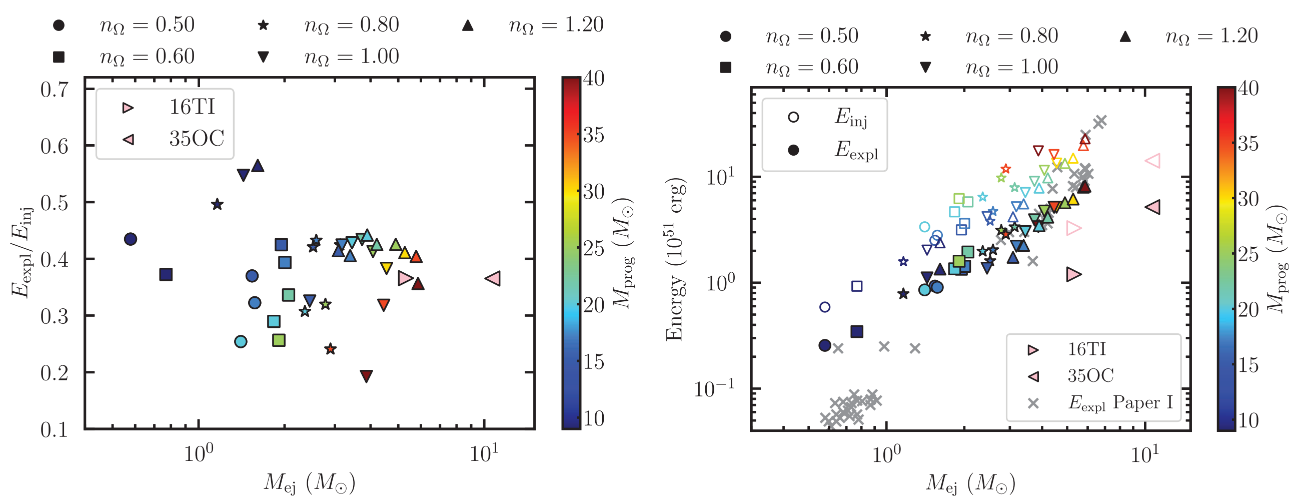

Figure 7. Left panel: the ratio of the explosion energy to the injected energy $E_{\rm expl}/E_{\rm inj}$ as a function of the ejecta mass $M_{\rm ej}$ for all the models studied in this work. Right panel: $E_{\rm expl}$ (filled markers) and $E_{\rm inj}$ (open markers) as functions of the ejecta mass $M_{\rm ej}$. Results for progenitors from Aguilera-Dena et al. (2020) with different degrees of rotation are distinguished by different markers, while the colour indicates the progenitor mass $M_{\rm prog}$. The right-pointing and left-pointing pink triangles are the results for the models `16TI` and `35OC` from Woosley & Heger (2006). The grey $\times$-markers show the results of $E_{\rm expl}$ obtained in Paper I for the model AD020x1.0.

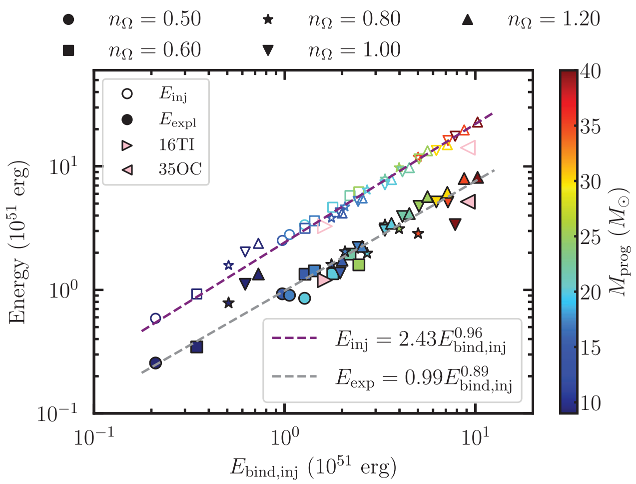

Figure 8. $E_{\rm expl}$ (filled markers) and $E_{\rm inj}$ (open markers) as functions of the binding energy evaluated at the injection time $E_{\rm bind,inj}$ for all the models studied in this work. The right-pointing and left-pointing pink triangles are the results for the models 16TI and 35OC from Woosley & Heger (2006). The right-pointing and left-pointing pink triangles are the results for the models 16TI and 35OC from Woosley & Heger (2006). The dashed purple line represents the linear regression $E_{\rm inj}$ and the dashed grey line the linear regression of $E_{\rm expl}$ for the models of Aguilera-Dena et al. (2020). The excluded models are not shown in this plot and are discussed in Appendix C. Results for progenitors with different angular velocities are distinguished by different markers, while the colour indicates the progenitor mass $M_{\rm prog}$.

space in the between would be filled by progenitors with initial mass ranging from 9 to 15 $\mathrm{M}_\odot$ or $n_\Omega = 0.7$. The distributions of $E_{\rm expl}$ and $E_{\rm inj}$ for the progenitor 16TI and 35OC also look continuous with respect to the ejecta mass and both the explosion and the injected energy are comparable to those measured for the models of Aguilera-Dena et al. (2020) with analogous $M_{\rm prog}$, but the points are located at higher values of $M_{\rm ej}$. For the 16TI we measure $E_{\rm expl} \approx 1.2 \times 10^{51}$ erg and $M_{\rm ej} \approx 5.3\,\mathrm{M}_\odot$ compared, for instance, to $E_{\rm expl} \approx 1.37 \times 10^{51}$ erg and $M_{\rm ej} \approx 2.37\,\mathrm{M}_\odot$ for AD015x1.5. For the 35OC progenitor, we instead measure $E_{\rm expl} \approx 5.2 \times 10^{51}$ erg and $M_{\rm ej} \approx 10.7\,\mathrm{M}_\odot$ while in the case of AD035x1.0 we find $E_{\rm expl} \approx 5.2 \times 10^{51}$ erg as well but $M_{\rm ej} \approx 4.3\,\mathrm{M}_\odot$.

The same figure also shows that $E_{\rm expl}$ and $M_{\rm ej}$ have a clear correlation with n_Ω, i.e. the faster the progenitor rotates, the larger $E_{\rm expl}$ and $M_{\rm ej}$ are. This is consistent with our expectation since a progenitor with higher values of n_Ω has a larger disc mass which is the source of the wind injection.

It is also noticeable that the distribution of the points obtained in this work varying the progenitor model covers a smaller interval of explosion energies than that presented in Paper I for different wind injection models that span from $\sim 5 \times 10^{49}$ to $\sim 3.4 \times 10^{52}$ erg. Additionally, in the present study, $E_{\rm expl}$ does not show a bimodal distribution for highly energetic and sub-energetic explosions. This confirms our hypothesis presented in Section 3.1 that the bimodal distribution obtained in Paper I is likely to be determined by the model for central engine employed. Since for this analysis, we employ the parameters that determine an energetic explosion of AD020x1.0 in Paper I, even changing the progenitor structure, the explosion would also belong to the same category.

In Fig. 8, we plot $E_{\rm inj}$ and $E_{\rm expl}$ as functions of the binding energy of the matter at the onset of the wind injection, $E_{\rm bind,inj}$, for all models. $E_{\rm inj}$ and $E_{\rm expl}$ increase approximately linearly with $E_{\rm bind,inj}$ and, specifically, the injected energy is always larger than the binding energy, as it is in the model 20_3.16_3.16_0.1_0.10. This confirms that in all the simulations, the explosion is driven by the same mechanism, i.e. by the ram pressure of the injected wind that dominates over that of the infalling matter, efficiently pushing forward the stellar envelope that expands without falling back. As a result, all the models experience an energetic explosion.

A good linear correlation between $E_{\rm expl}$ and $E_{\rm bind,inj}$ is reasonable: the engine of the explosion has to provide the energy similar to $E_{\rm bind,inj}$ for a successful explosion. When the energy with the order of $E_{\rm bind,inj}$ is injected, the stellar envelope becomes unbound by the injected wind. Hence, the mass infall to the central BH-disc system and the new energy injection are suppressed. The explosion energy is thus likely to be regulated by the order of $E_{\rm bind,inj}$. Comparing the injected energy of the models 16TI and 35OC with that measured in for the progenitor of Aguilera-Dena et al. (2020) for give $E_{\rm bind,inj}$, we notice that it is slightly smaller in the case of 16TI and 35OC. This difference can relate to the difference in the progenitor features and to the simple model we used. Therefore the fits shown in Fig. 8 are made using only the results for the progenitors of Aguilera-Dena et al. (2020).

3.2 Comparison with the observations

In this section, we compare the ejecta properties obtained in our simulation with the observational data. Fig. 9 presents the distribution of our model in the $E_{\rm expl}$–$M_{\rm ej}$ plane (filled markers) along with the observational data for Ic-BL SNe taken from Taddia et al. (2019) and for stripped-envelope SNe, including Type Ic-BL SNe from Gomez et al. (2022) (open markers). We additionally display the results of some general relativistic neutrino-radiation viscous-hydrodynamics simulations obtained using different progenitors: from Fujibayashi et al. (2024) for progenitors with $M_{\rm prog}$ =20, 35, and 45 $\mathrm{M}_\odot$ of Aguilera-Dena et al. (2020) and different degrees of rotation $n_\Omega = 0.6$, 0.8, 1.0, 1.2 and from Just et al. (2022) and Dean & Fernández (2024a) for 16TI and 35OC models in Woosley & Heger (2006). In Fig. 9, we focus on the dependence of the explosion on the progenitor mass $M_{\rm prog}$ indicated by the colour of the markers and on the magnitude of the angular velocity n_Ω distinguished by the marker shape.

Comparing our numerical results with the observational data, we find that our results agree with some range of the observational data. However, we also find that, despite the wide-ranging variations of $M_{\rm prog}$ and n_Ω, the explosion energy distributes along a trend and does not show the extended distribution made by observational data. In other words, the explosion energy and the ejecta mass are more strongly correlated in our simulations than in the observational data provided by Taddia et al. (2019) and Gomez et al. (2022). A similar tight correlation between $E_{\rm expl}$ and $M_{\rm ej}$ was also found in our previous work for the model AD020x1.0 as indicated by the $\times$-markers in the right panel of Fig. 9 (see also fig. 11 in Paper I).

We find that the observational data points with $M_{\rm ej} \gtrsim 10\,\mathrm{M}_\odot$ are hardly reproduced with the progenitor models of Aguilera-Dena et al. (2020). The reason is just that the available mass for the ejecta, i.e. the pre-collapse stellar mass minus BH mass at the disc formation (see the upper panel of Fig. 5 and upper panel of fig. 1 in Aguilera-Dena et al. 2020), is at most $\sim 10\,\mathrm{M}_\odot$. The events with $M_{\rm ej} \gtrsim 10\,\mathrm{M}_\odot$ may have originated from the stars that have larger available mass, i.e. with larger envelope mass or faster rotation, in the context of a collapsar scenario.

Our speculation is supported by the points obtained by numerical simulations (Dean & Fernández 2024a; Just et al. 2022) that use

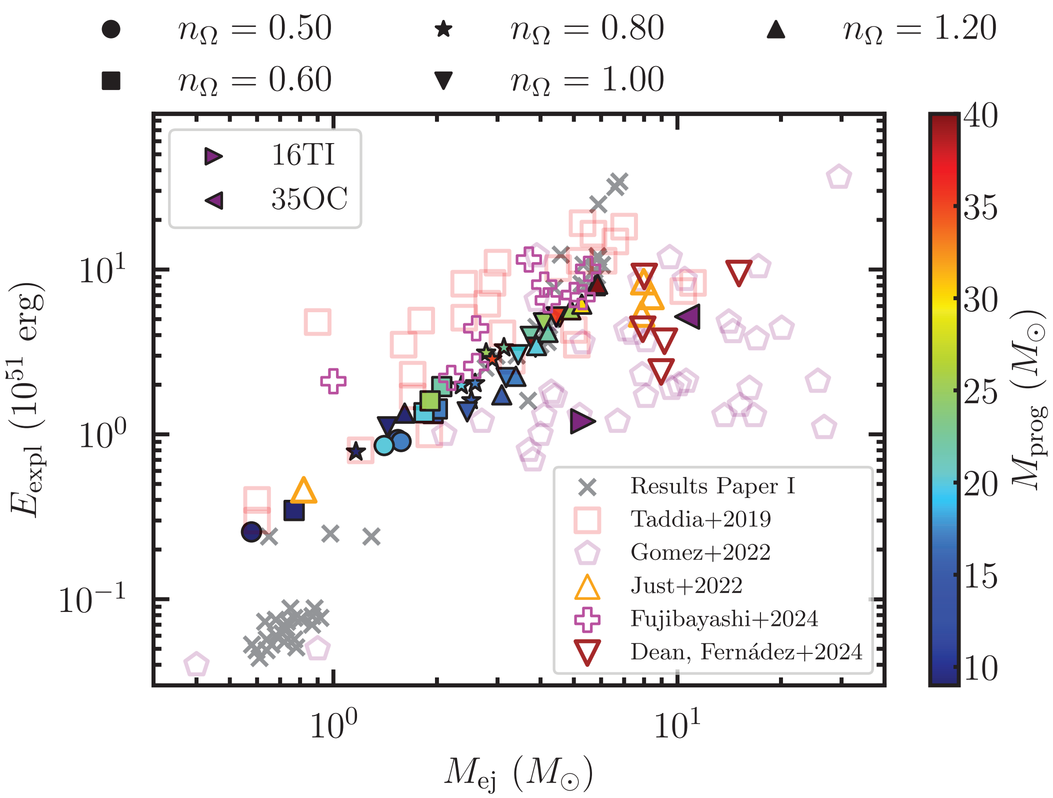

Figure 9. Parameter dependence with respect to the observable pair of explosion energy $E_{\rm expl}$ and ejecta mass $M_{\rm ej}$. Results for progenitors from Aguilera-Dena et al. (2020) with different degrees of rotation are distinguished by different markers, while the colour indicates the progenitor mass $M_{\rm prog}$. The grey $\times$-markers show our results obtained in Paper I for the model AD020x1.0. The open markers display the observational data for stripped-envelope SNe, some of which are Type Ic-BL SNe, taken from Taddia et al. (2019) and Gomez et al. (2022). The up-pointing triangles display the results of Just et al. (2022) from neutrino-radiation viscous-hydrodynamics simulations with the progenitors `16TI`. The magenta plus-sign denotes the results obtained in a general relativistic neutrino-radiation viscous-hydrodynamics simulation for progenitors with $M_{\rm prog} = 20,\ 35,\ 45\,{\rm M}_{\odot}$ and $n_{\Omega} = 0.6,\ 0.8,\ 1.0,\ 1.2$ (Fujibayashi et al. 2024). The down-pointing triangles show the results of Dean & Fernández (2024a) from neutrino-radiation viscous-hydrodynamics simulations with the progenitors `16TI` and `35OC`. For the same models `16TI` and `35OC` we perform additional simulations displayed in the figure with a right-pointing and a left-pointing purple arrow, respectively.

faster rotating pre-collapse structure (`16IT` and `35OC`; Woosley & Heger 2006). Their ejecta mass is systematically higher than those of our result. This indicates that the tight correlation found in our result may stem from our limited choice of the progenitor structure, and we could reproduce events with $M_{\rm ej} \gtrsim 10\,{\rm M}_{\odot}$ with more massive or faster rotating progenitors.

We also note that the results obtained in Fujibayashi et al. (2024) are well aligned with the outcomes of our simulations showcased in Fig. 9, while the results in Dean & Fernández (2024a) and Just et al. (2022) are located in the regime with systematically higher values of $M_{\rm ej}$. The better agreement with Fujibayashi et al. (2024) could also be due to the choice of the progenitor models: Fujibayashi et al. (2024) also use the same progenitor stars as ours. This fact may also support the above speculation.

To confirm our speculation, we perform additional simulations using progenitor models `16TI` and `35OC`. For the `16TI` we measure the ejecta mass of $M_{\rm ej} \approx 5.3\,{\rm M}_{\odot}$ and en explosion energy $E_{\rm expl} \approx 1.2 \times 10^{51}$ erg, while for the `35OC` progenitor $M_{\rm ej} \approx 10.7\,{\rm M}_{\odot}$ and $E_{\rm expl} \approx 5.2 \times 10^{51}$ erg. For these models we measure an $E_{\rm expl}$ similar to that of the progenitor from Aguilera-Dena et al. (2020) with the same mass, but the point distribution `16TI` and `35OC` is located at higher $M_{\rm ej}$, in qualitative agreement with the results obtained by Dean & Fernández (2024a). The difference between the values of $E_{\rm expl}$ we measured for `16TI` and `35OC` and those obtained by `16TI` and `35OC` can be attributed to the simple wind model we used where the wind parameters are fixed throughout the whole simulation.

3.3 Prediction on the explosion energy

It would be advantageous to have a tool useful for choosing a potential progenitor based on some requirements for the outcomes before performing any simulation. We provide such a tool using the binding energy of the outer layers $E_{\rm ol}$ (ol = outer layers), which is defined as:

$$E_{\rm ol} = \frac{G M_{\rm ol} M^{\rm df}_{\rm encl}}{R^{\rm df}_{\rm encl}}\,, \tag{12}$$

where $M^{\rm df}_{\rm encl}$ is the mass coordinate at which the specific angular momentum is equal to that of ISCO for a BH with the same mass and angular momentum of their enclosed values, i.e. the estimated BH mass at the disc formation. $R^{\rm df}_{\rm encl}$ is the radius of the mass coordinate $M^{\rm df}_{\rm encl}$, and $M_{\rm ol}$ is the mass outside the same mass coordinate. This quantity would provide an estimate of available energy by the accretion of the outer layer to the disc.

In Fig. 10, we show the relation between $E_{\rm expl}$ and $E_{\rm ol}$, for both the model from Aguilera-Dena et al. (2020) and the `16TI` and `35OC` of Woosley & Heger (2006) (right and left-pointing pink triangles, respectively). In Fig. 10, we also plot the line of $E_{\rm expl} = E_{\rm ol}$ (purple dashed line in the figure) to provide an order of magnitude estimate

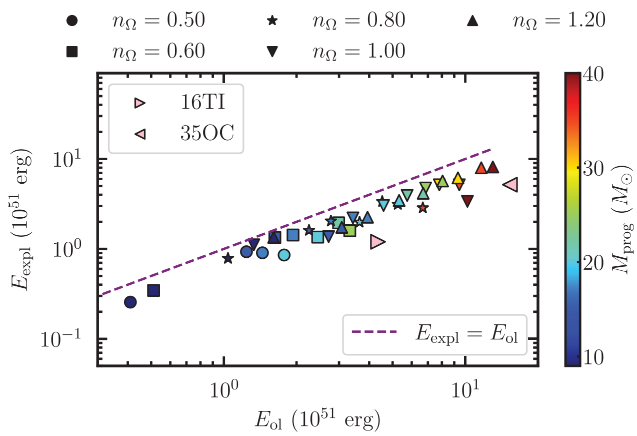

Figure 10. Explosion energy $E_{\rm expl}$ as a function of the binding energy of the outer layers in the pre-collapse ($E_{\rm ol}$) for the models from Aguilera-Dena et al. (2020) and Woosley & Heger (2006). $E_{\rm ol}$ is a measure of the compactness of the entire star. The dashed purple line shows $E_{\rm expl} = E_{\rm ol}$ to provide an order of magnitude for the explosion energy. Results for progenitors with different angular velocity are distinguished by different markers, while the colour indicates the progenitor mass $M_{\rm prog}$. The right-pointing and left-pointing pink triangles are the results for the models `16TI` and `35OC` from Woosley & Heger (2006).

of the explosion energy considering only the pre-collapse conditions. The linear line of $E_{\rm expl} = E_{\rm ol}$ well reproduces the relation between $E_{\rm expl}$ and $E_{\rm ol}$ we obtained within a factor 2 (with the difference between $E_{\rm expl}$ obtained in our results and $E_{\rm ol}$ ranging from to 16 per cent–60 per cent of $E_{\rm ol}$). The somewhat smaller $E_{\rm expl}$ than $E_{\rm ol}$ indicates that not all the gravitational binding energy of the outer layer is used for the explosion.

Considering the relation between $E_{\rm expl}$ and $E_{\rm ol}$ for the progenitor stars `16TI` and `35OC`, we notice that the points lay outside the trend described by the distribution of the progenitors from Aguilera-Dena et al. (2020). Therefore the relation we found between $E_{\rm ol}$ and $E_{\rm expl}$ applies only to the models of Aguilera-Dena et al. (2020) with a moderate modification of rotation.

3.4 ^{56}Ni production

In this section, we analyse the results of the ^{56}Ni production and the way in which it correlates with the progenitor mass and its angular velocity. By doing that, we aim to ascertain whether it is feasible to replicate observational data such as those presented by Taddia et al. (2019) and Gomez et al. (2022), especially for the high-energy SNe ($E_{\rm expl} \gtrsim 10^{52}$ erg).

The data used in our ^{56}Ni calculations are summarized in Table 1. The table includes, starting from the fifth column: the mass of ejecta component originating from the injected matter (i.e. from the disc) $M^{\rm inj}_{\rm ej}$, the total mass experiencing temperature higher than 5 GK, $M_{>5\,\rm GK}$, (5 GK is the threshold above which the ^{56}Ni production primarily occurs), the mass of the stellar component experiencing temperature higher than 5 GK, $M^{\rm stellar}_{\rm ej,>5GK}$, and the ratio between the injected matter that is estimated to experience temperature higher than 5 GK and the total injected mass $M^{\rm inj}_{>5\rm GK}/M^{\rm inj}$. For the values of $M_{>5\,\rm GK}$ and $M^{\rm stellar}_{\rm ej,>5GK}$, also the number of tracers is shown in parenthesis. In this work, we employ tracer particles to estimate the ^{56}Ni mass synthesized in the matter originating from the stellar envelope under the assumption that it is produced by the fluid elements experiencing temperatures higher than 5 GK. We make this approximation without computing the whole nucleosynthesis because we found that the ejecta mass is dominated by the injected matter, which is larger than $M^{\rm stellar}_{\rm ej,>5GK}$ by more than one order of magnitude. For this component, as mentioned in Section 2 we estimate the mass of ^{56}Ni by evaluating the temperature of the disc when the matter is injected (see Appendix B). Therefore, we roughly estimate the mass of ^{56}Ni in the ejecta, $M_{\rm ej,Ni}$ as $M_{\rm ej,Ni} = M^{\rm stellar}_{\rm ej,>5GK} + M^{\rm inj}_{\rm ej,>5GK}$, where $M^{\rm inj}_{\rm ej,>5GK}$ is $M^{\rm inj}_{\rm ej}$ multiplied by the ratio $M^{\rm inj}_{>5\rm GK}/M^{\rm inj}$.

With this approximation, $M_{\rm ej,Ni}$ is found to represent the ∼13–41 per cent of the total ejecta mass, with the lowest amount of ∼0.19 M$_\odot$ produced in the progenitor AD009x0.8 and the largest of ∼2.3 M$_\odot$ for the model AD040x1.2.

Fig. 11 shows for all models our estimates of the ^{56}Ni mass produced in the whole ejecta $M_{\rm ej,>5\,GK}$ (open markers) and that originating from the stellar component $M^{\rm stellar}_{\rm ej,>5\,GK}$ (filled markers) as a function of the explosion energy (left panel) and of the average ejecta velocity (right panel). In addition to the results of our simulations, in the plots we include the observational data for Type Ic-BL SNe taken from Taddia et al. (2019) and for stripped-envelope SNe, including Ic-BL SNe, taken from Gomez et al. (2022). Furthermore we also show the ^{56}Ni mass obtained by Fujibayashi et al. (2024) and by Dean & Fernández (2024a).

Fig. 11 highlights how strongly the component of the ejecta originating from the injected matter dominates the estimate of the total ^{56}Ni mass produced in all models. It also shows that $M_{\rm ej,>5\,GK}$ tends to increase with $E_{\rm expl}$ (or with respect to $v_{\rm ej}$). The dependence of $M_{\rm ej,>5\,GK}$ on $E_{\rm expl}$ is reasonable: more massive and faster rotating progenitors have larger values of $E_{\rm expl}$ and $M_{\rm ej}$ due to the larger disc mass (we discussed it in Section 3.1; see also Fig. 7) and $M_{\rm disc}$ is the source of the injected matter, a significant fraction of which is here considered to become ^{56}Ni. Even though not as linearly as $M_{\rm ej,>5\,GK}$, also $M^{\rm stellar}_{\rm ej,>5\,GK}$ roughly increases with $E_{\rm expl}$ in the left panel of Fig. 11. This is because the energy injection occurs in similar time-scale $\sim t_{\rm w}$. This leads to the higher energy injection rate $E_{\rm inj}/t_{\rm w}$ for higher $E_{\rm expl}$ models, and thus, more matter tends to experience higher temperature (see Suwa, Tominaga & Maeda 2019 for the positive correlation between the energy injection rate and temperature that the ejecta experience).

The left panel of Fig. 11 shows that our numerical estimates of the ^{56}Ni mass are in fair agreement with the relation between $M_{\rm ej,Ni}$ and $E_{\rm expl}$ in the observational data and with the results obtained by both Fujibayashi et al. (2024) and Dean & Fernández (2024a). We can reproduce at least some class of SNe Ic-BL with, basically, only the exclusion of the observed explosions with $E_{\rm expl} < 10^{50}$ or $E_{\rm expl} > 10^{52}$ erg. The capability of reproducing the observational data is the result of the calibration of the wind parameter with the numerical results of Fujibayashi et al. (2024). Fig. 11 shows that such calibration allows us to be in good agreement with a wide range of energetic SNe with a broad range of progenitor mass. Comparing our results with the observational data in the right panel of Fig. 11, we also have to note that lower velocity SNe of Gomez et al. (2022) are likely to be normal SNe Ic resulting from the heating by neutrinos emitted from the PNS, which we are not trying to reproduce with our models.

Focusing on the right panel of Fig. 11, we observe that the total ^{56}Ni mass produced in our simulations is in fair agreement with the observational data in the range of the ejecta velocity we measured, i.e. $v_{\rm ej} \sim 6\times10^3$–$12\times10^3$ km s^{-1}. However, our simulation results are less scattered than the observational data, which spread up to $\sim 25\times10^3$ km s^{-1} (excluding the normal SNe Ic from Gomez et al.

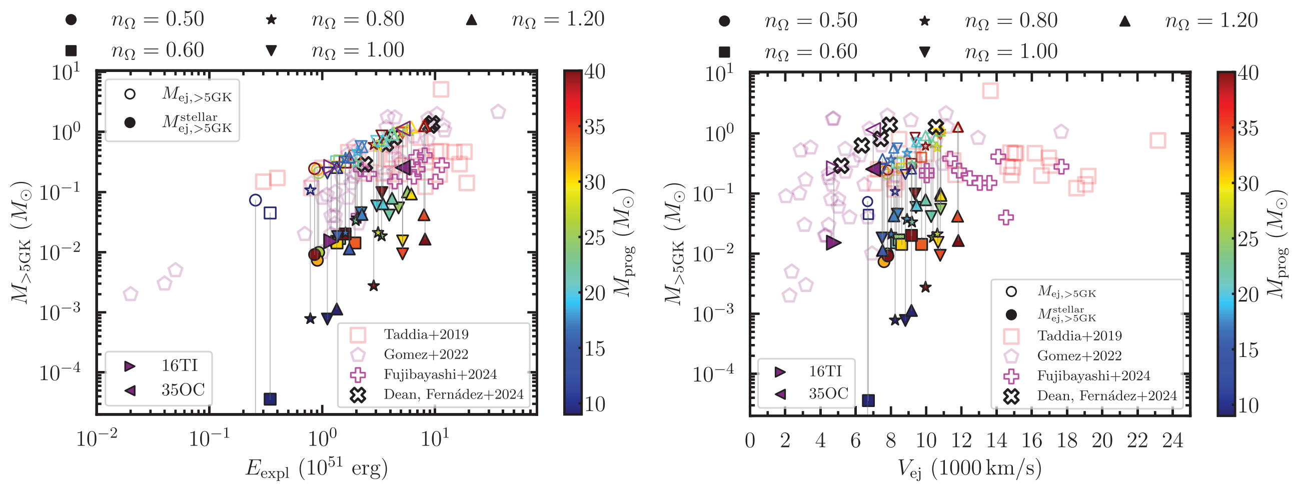

Figure 11. Relations between the explosion energy and the ^{56}Ni mass (left) and between the average velocity of the ejecta and the ^{56}Ni mass (right). Each grey line connects $M^{\rm stellar}_{\rm ej,>5GK}$ (triangles) and $M_{\rm ej,>5GK} = M^{\rm stellar}_{\rm ej,>5GK} + M^{\rm inj}_{\rm ej,>5GK} * M^{\rm inj}_{>5\rm GK}/M^{\rm inj}$ (down-pointing triangles) of the same model to show the possible range of ^{56}Ni mass. For the models from Aguilera-Dena et al. (2020), results for progenitors with different angular velocity are distinguished by different markers, while the colour indicates the progenitor mass $M_{\rm prog}$. The results with the models `16TI` and `35OC` are displayed with a right-pointing and a left-pointing purple arrow, respectively. The open markers display the observational data for stripped-envelope SNe, some of which are Type Ic-BL SNe, taken from Taddia et al. (2019) and Gomez et al. (2022). The magenta plus-sign denotes the results obtained in a general relativistic neutrino-radiation viscous-hydrodynamics simulation for progenitors with $M_{\rm prog} = 20,\ 35,\ 45\,{\rm M}_\odot$ and $n_\Omega = 0.6,\ 0.8,\ 1.0,\ 1.2$ (Fujibayashi et al. 2024). The open black x-markers show the results of Dean & Fernández (2024a) from neutrino-radiation viscous-hydrodynamics simulations with the progenitors `16TI` and `35OC`.

(2022) and focusing on the high-energy distribution). Considering the fact that the results of Fujibayashi et al. (2024) extend to higher velocity up to 18×10^3 km s^{-1}, the reasonable reason for this can be attributed to our choice of a simple wind model; for instance, in the present set-up, the wind time-scale $t_{\rm w}$ and the accretion time-scale $t_{\rm acc}$ are set constant and do not depend on the BH-disc properties, e.g. the Keplerian time at the typical disc radius $\propto \sqrt{M_{\rm BH}/{r_{\rm disc}}^3}$. We find that the higher progenitor mass tends to result in high ejecta velocity in Fujibayashi et al. (2024). This indicates that our wind parameter set chosen in this study is somewhat different for higher progenitor mass. Considering that Paper I achieved a high ejecta velocity $\sim 20 \times 10^3$ km s^{-1} with longer wind time-scale $t_{\rm w} = 10$ s for $M_{\rm prog} = 20\,{\rm M}_\odot$ star, the disc formed in the collapse of a more massive progenitor may have a longer wind time-scale.

In Fig. 11, it is possible to observe a dependence of the total ^{56}Ni mass in the ejecta on the progenitor mass and angular velocity. To better appreciate it, in Fig. 12, we plot $M_{\rm ej,Ni}$ as a function of $M_{\rm prog}$ for all models, distinguishing them also by their degree of rotation with different markers and colours. The figure shows a specific correlation among $M_{\rm ej,Ni}$, $M_{\rm prog}$, and n_Ω. More massive and faster rotating progenitors tend to produce more ^{56}Ni in the ejecta. The explanation for this behaviour can be the same as speculated above to describe the relation between $M_{\rm ej,Ni}$ and $E_{\rm expl}$: more massive and faster rotating progenitors have a larger disc mass, which is the source of the wind injection and ^{56}Ni mass.

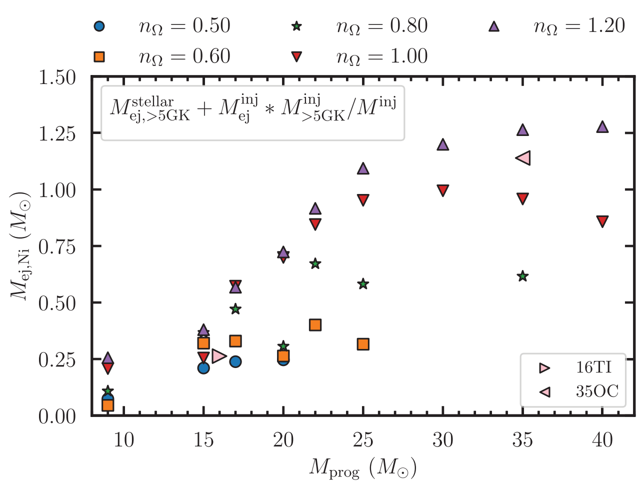

Figure 12. Correlation between the ^{56}Ni mass and the progenitor mass with a variety of progenitor angular velocity. For the progenitors of Aguilera-Dena et al. (2020), markers and colours distinguish the values of n_Ω. The results with the models `16TI` and `35OC` are displayed with a pink right-pointing and a left-pointing purple arrow, respectively.

4 DISCUSSION

4.1 Variety of disc wind-driven explosion

The present analysis of our results shows a large variety of ejecta mass with $M_{\rm ej}$ going from $\sim 0.6\,{\rm M}_\odot$ for the model AD009x0.5 to $> 10\,{\rm M}_\odot$ for the progenitor `35OC` and a large variety of explosion energy with $E_{\rm expl}$ spanning from $\sim 0.3 \times 10^{51}$ erg for the model AD009x0.5 to $\sim 8 \times 10^{51}$ erg for AD040x1.2. Focusing on the results obtained using the models of Aguilera-Dena et al. (2020), Fig. 7 shows a monotonic trend of our results, where $E_{\rm expl}$ and $M_{\rm ej}$ increase with the progenitor mass and the initial degree of the rotation. The effect of the progenitor mass on the outcome of the explosion can be explained considering that, typically, more massive stars are supposed to have a more compact envelope (in terms of M_*/R_*), resulting in higher mass-infall rates, which provides a larger amount of matter for the disc formation and a larger energy budget for explosion energy. The impact of the initial magnitude of the rotation, after the BH formation, on the explosion energy, and on the ejecta mass is investigated by fully general relativistic radiation viscous hydrodynamics in Fujibayashi et al. (2024). They showed that a star with a fast rotation can yield a more energetic explosion and enhance mass ejection. Our present models approximately reproduce their findings.

Another interesting result, as mentioned in Section 3.2, is that we found a stronger correlation between $E_{\rm expl}$ and $M_{\rm ej}$ in our models than in the observational data. We also hardly reproduced data points with $M_{\rm ej} \gtrsim 10\,{\rm M}_\odot$ (refer to Fig. 9). As discussed in Section 3.2, they may be partially due to the choice of the progenitor models. In the same subsection, we demonstrated that using the faster rotating pre-collapse structures `16TI` and `35OC`, also employed by Dean & Fernández (2024a), we could actually reproduce samples with $M_{\rm ej} \gtrsim 10\,{\rm M}_\odot$. This indicates that there may be a wider variety of ejecta properties than we find in this work, which stems from the difference in the mass and angular momentum distributions of the pre-collapse stellar structure.

Another possible reason for the tight correlation can be attributed to the simple wind model we use, in which the wind parameters, e.g. the wind and accretion time-scales, are fixed throughout the whole simulation. As mentioned in Section 2.5, this hypothesis is supported by the comparison to the results obtained in Fujibayashi et al. (2024). The higher mass progenitor models tend to result in higher velocities and, thus, higher explosion energies than we find with the same progenitors (see also Fig. 7). This indicates that the relevant time-scale for the wind injection may be different for different progenitors. This is reasonable because the different mass and angular momentum distribution of pre-collapse structure naturally leads to the different characteristics of the BH-disc system, e.g. different Keplerian time-scale. We would, then, conclude that it may be possible to reproduce the variety of the observational data by the combination of the wide variety of the progenitor structure and more consistent modelling of the wind injection. In reality, the wind injection would occur after the efficiency of neutrino cooling compared to the viscous heating in the disc drops (Fujibayashi et al. 2024); both $t_{\rm w}$ and $t_{\rm acc}$ should depend sensitively on the neutrino cooling. Therefore, it is necessary to construct a more sophisticated wind injection model that consistently captures the physical processes during both the neutrino-dominated accretion flow (Popham et al. 1999; Kohri et al. 2005) and the advection-dominated accretion flow (Narayan & Yi 1994; Hayakawa & Maeda 2018) phases in the specific case of a viscosity-driven wind explosion. We leave the construction of the model and the investigation with it for future work.

4.2 The effect of GRB jet

One of our aims for future studies and a possible use of this work is to connect the progenitor and the failed CCSN with a GRB that could be launched in such a scenario if a relativistic jet is produced (see e.g. Aloy et al. 2000; Izzard et al. 2004; Zhang, Woosley & Heger 2004; Mizuta et al. 2006; Gottlieb et al. 2022; Shibata et al. 2024 for simulation works with various sophistication). Performing relativistic-hydrodynamic simulations with the inclusion of relativistic jets would be an interesting case to investigate. As a matter of fact, if we also consider in our model a large dimensionless spin of the BH and an electromagnetic fields, then we could have the formation of an energetic jet or outflow along the spin axis of the BH determined by the Blandford–Znajek effect (see Blandford & Znajek 1977). Consequently, if a relativistic jet is formed, the energy budget for the explosion and the ^{56}Ni production may increase because more energy is injected into the stellar matter. Several works have already studied this scenario, hence proposing that the jet and associated cocoon drive the stellar explosion and that it can launch a GRB (e.g. Hjorth et al. 2003; Stanek et al. 2003; Lazzati et al. 2012; Eisenberg, Gottlieb & Nakar 2022; Suzuki & Maeda 2022). Tominaga et al. (2007) and Tominaga (2008) studied the jet-induced explosions of a Population III $40\,{\rm M}_\odot$ star and suggested a correlation between GRBs with and without bright SNe and the energy deposition rate $\dot{E}_{\rm dep}$ (see also Maeda & Nomoto 2003; Nagataki, Mizuta & Sato 2006). They found that explosion with high energy ($\dot{E}_{\rm dep} \gtrsim 6 \times 10^{52}$ erg) can synthesize a large amount of ^{56}Ni ($\gtrsim 0.1\,{\rm M}_\odot$) resulting consistent with GRB-SNe. Contrarily, if the explosion deposition rate is low ($\dot{E}_{\rm dep} \lesssim 3 \times 10^{51}$ erg), they measured a low ejected ^{56}Ni mass ($\lesssim 10^{-3}\,{\rm M}_\odot$) comparable to that observed in GRBs without SN brightening (like GRB060505 and GRB0606014). The GRB-SN mechanism was also found to be strongly sensitive to the angular momentum of the progenitor, but unaffected by its mass (Hayakawa & Maeda 2018). Considering the previous works, then, one of our follow-up studies will be performing relativistic-hydrodynamic simulations that incorporate the injection of relativistic jets.

5 SUMMARY AND CONCLUSIONS

In this work, we extended our previous study of the hydrodynamics and nucleosynthesis for the explosion of massive stars in the collapsar scenario by performing a series of two-dimensional, Newtonian simulations of progenitor models with different characteristics. Specifically, we selected nine models from Aguilera-Dena et al. (2020) sampled in the range of $M_{\rm prog} = 9$–$40\,{\rm M}_\odot$. We, then, studied them at five different angular velocities (see Section 2). To further investigate the dependence of the ejecta properties on the progenitor structure, we additionally performed two simulations with the models `16TI` and `35OC` from Woosley & Heger (2006) that have a larger angular momentum than those of Aguilera-Dena et al. (2020) for a given mass (for these simulations we used the original angular velocity profile). For these simulations, we worked with the open-source multidimensional hydrodynamics code ATHENA++ solving the axisymmetric gravitational potential as in Paper I. We also used the same model for the central engine that is supposed to evolve the BH and the disc with the transfer of matter and angular momentum and that also includes the disc wind formation and injection.

Our main aim was to investigate the effect of the progenitor structure on the properties of the ejecta. In order to focus our investigation on the effect of the progenitor structure on the faith of the evolution, we fix the parameters of the wind injection model so that the results of the explosion of the AD020x1.0 progenitor are similar to those obtained by Fujibayashi et al. (2023) for the same star. In all our models, the disc-driven explosion results in an explosion with $E_{\rm expl}$ ranging from 0.3×10^{51} erg for the model AD009x0.5 to $> 8 \times 10^{51}$ erg for the model AD040x1.2 for the progenitor models of Aguilera-Dena et al. (2020). For the progenitor models of Woosley & Heger (2006), the explosion energy is comparable for a given progenitor mass, but the ejecta mass is larger because they have a larger available mass (the pre-collapse stellar mass minus BH mass at the disc formation), determined by a faster rotation and a larger initial envelope mass. Comparing the progenitors with $M_{\rm prog} = 35\,{\rm M}_\odot$ from Aguilera-Dena et al. (2020) and Woosley & Heger (2006), we measured $M_{\rm ej} = 4.3\,{\rm M}_\odot$ for AD035x1.0 while $M_{\rm ej} = 10.67\,{\rm M}_\odot$ in the case of `35OC`.

Analysing the impact of the progenitor model and its rotation on the final ejecta, we found that more massive stars reach higher explosion energy because of a higher mass-infall rate that supplies a larger amount of matter to form the disc and, therefore, a higher thermal energy budget for the explosion energy. Our results also show that faster rotating progenitors experience more energetic explosions due to a larger disc mass.

We find that the distribution of explosion energy and ejecta mass has a fair agreement with the observed distribution of SNe Ic-BL. This indicates that such an energetic explosion would be driven indeed by the disc wind in collapsars. We also find a strong correlation between the explosion energy and the binding energy of the outer layer of the star, $E_{\rm ol}$. We provided a function of $E_{\rm ol}$ to predict the explosion energy only with the information of the pre-collapse star.

As for the analysis of the ^{56}Ni production, in our simulations, $M_{\rm ej}^{\rm inj}$ mainly determines the estimate of the total mass of ^{56}Ni synthesized in the ejecta as it is more than one order of magnitude larger than $M_{\rm ej,>5GK}^{\rm stellar}$. Due to the predominance of $M_{\rm ej}^{\rm inj}$, for which the complete thermodynamical history is not available, we provided only a rough estimate of $M_{\rm ej,Ni}$. None the less, the distribution of our estimate of the ^{56}Ni mass can broadly explain the relation between $M_{\rm Ni}$ and $E_{\rm expl}$ of the observational data for stripped-envelope SNe (some of which are Ic-BL SNe) taken from Taddia et al. (2019) and Gomez et al. (2022). We also found a correlation between the ^{56}Ni mass and the progenitor's mass and angular velocity, i.e. more massive and faster rotating stars produce more ^{56}Ni.

We also found that our results on the explosion energy and ^{56}Ni mass agree approximately with those obtained by more detailed simulations (Fujibayashi et al. 2024; Dean & Fernández 2024a). This suggests that our rather simple hydrodynamics model captures the essence of the explosion mechanism in the collapsar scenario and is useful for interpreting the observational data. Yet, we found a tighter correlation of $E_{\rm expl}$ and $M_{\rm ej}$ than those of the observational data (Taddia et al. 2019 and Gomez et al. 2022). It is partially because of the limited class of progenitor structure. Another reason is likely to be the simple modelling of wind injection employed in this study (see Section 2.5). We will sophisticate our current wind injection model to capture the relevant physical processes consistently and further investigate the collapsar disc wind scenario in the future.

ACKNOWLEDGEMENTS

We want to thank David Aguilera-Dena for providing his stellar evolution model and Kengo Tomida for his help and suggestions in using ATHENA++. We are thankful for the useful and constructive discussion we had with Ayako Ishii. We also want to thank the anonymous referee for the comments that improved the manuscript. This study was supported in part by Grants-in-Aid for Scientific Research of the Japan Society for the Promotion of Science (JSPS, nos JP22K20377 and JP23H04900). Numerical computation was performed on Sakura cluster at Max Planck Computing and Data Facility.

DATA AVAILABILITY

The data will be shared on reasonable request to the corresponding author.

REFERENCES

Aguilera-Dena D. R., Langer N., Antoniadis J., Müller B., 2020, ApJ, 901, 114
Aloy M. A., Müller E., Ibáñez J. M., Martí J. M., MacFadyen A., 2000, ApJ, 531, L119
Bardeen J. M., Press W. H., Teukolsky S. A., 1972, ApJ, 178, 347
Blandford R. D., Znajek R. L., 1977, MNRAS, 179, 433
Bollig R., Yadav N., Kresse D., Janka H.-T., Müller B., Heger A., 2021, ApJ, 915, 28
Bruenn S. W. et al., 2023, ApJ, 947, 35
Bugli M., Guilet J., Obergaulinger M., Cerdá-Durán P., Aloy M. A., 2019, MNRAS, 492, 58
Burrows A., Vartanyan D., 2021, Nature, 589, 29
Burrows A., Dessart L., Livne E., Ott C. D., Murphy J., 2007, ApJ, 664, 416
Campana S. et al., 2006, Nature, 442, 1008
Dean C., Fernández R., 2024a, Phys. Rev. D, 109, 083010
Dean C., Fernández R., 2024b, Phys. Rev. D, 110, 083024
Eisenberg M., Gottlieb O., Nakar E., 2022, MNRAS, 517, 582
Ertl T., Janka H. T., Woosley S. E., Sukhbold T., Ugliano M., 2016, ApJ, 818, 124
Fujibayashi S., Sekiguchi Y., Shibata M., Wanajo S., 2023, ApJ, 956, 100
Fujibayashi S., Lam A. T.-L., Shibata M., Sekiguchi Y., 2024, Phys. Rev. D, 109, 023031
Galama T. J. et al., 1998, Nature, 395, 670
Gomez S., Berger E., Nicholl M., Blanchard P. K., Hosseinzadeh G., 2022, ApJ, 941, 107
Gottlieb O., Lalakos A., Bromberg O., Liska M., Tchekhovskoy A., 2022, MNRAS, 510, 4962
Grimmett J. J., Müller B., Heger A., Banerjee P., Obergaulinger M., 2021, MNRAS, 501, 2764
Hayakawa T., Maeda K., 2018, ApJ, 854, 43
Hjorth J. et al., 2003, Nature, 423, 847
Issa D., Gottlieb O., Metzger B., Jacquemin-Ide J., Liska M., Foucart F., Halevi G., Tchekhovskoy A., 2024, preprint (arXiv:2410.02852)
Izzard R. G., Tout C. A., Karakas A. I., Pols O. R., 2004, MNRAS, 350, 407
Janka H.-T., Hanke F., Hüdepohl L., Marek A., Müller B., Obergaulinger M., 2012, Prog. Theor. Exp. Phys., 2012, 01A309
Janka H.-T., Melson T., Summa A., 2016, Annu. Rev. Nucl. Part. Sci., 66, 341–375
Just O., Aloy M. A., Obergaulinger M., Nagataki S., 2022, ApJ, 934, L30
Kohri K., Narayan R., Piran T., 2005, ApJ, 629, 341
Kumar P., Zhang B., 2015, Phys. Rep., 561, 1
Kumar P., Narayan R., Johnson J. L., 2008, MNRAS, 388, 1729
Kuroda T., Arcones A., Takiwaki T., Kotake K., 2020, ApJ, 896, 102
Kuroda T., Fischer T., Takiwaki T., Kotake K., 2022, ApJ, 924, 38
Lazzati D., Morsony B. J., Blackwell C. H., Begelman M. C., 2012, ApJ, 750, 68
MacFadyen A., Woosley S., 1999, ApJ, 524, 262
Maeda K., Nomoto K., 2003, ApJ, 598, 1163
Menegazzi L. C., Fujibayashi S., Takahashi K., Ishii A., 2024, MNRAS, 529, 178
Metzger B. D., Giannios D., Thompson T. A., Bucciantini N., Quataert E., 2011, MNRAS, 413, 2031
Mezzacappa A., 2020, Proc. IAU Vol. 362, The Predictive Power of Computational Astrophysics as a Discovery Tool. Cambridge University Press, p. 215
Miller J. M., Sprouse T. M., Fryer C. L., Ryan B. R., Dolence J. C., Mumpower M. R., Surman R., 2020, ApJ, 902, 66
Mizuta A., Yamasaki T., Nagataki S., Mineshige S., 2006, ApJ, 651, 960
Mösta P., Ott C. D., Radice D., Roberts L. F., Schnetter E., Haas R., 2015, Nature, 528, 376–379
Müller B., Heger A., Liptai D., Cameron J. B., 2016, MNRAS, 460, 742
Nagataki S., Mizuta A., Sato K., 2006, ApJ, 647, 1255
Narayan R., Yi I., 1994, ApJ, 428, L13
Obergaulinger M., Aloy M. Á., 2020, MNRAS, 492, 4613
Piran T., 2004, Rev. Mod. Phys., 76, 1143
Popham R., Woosley S. E., Fryer C., 1999, ApJ, 518, 356
Rahman N., Janka H.-t., Stockinger G., Woosley S. E., 2023, Proc. Sci., FAIR Next Generation Scientists - 7th Edition Workshop. SISSA, Trieste, PoS#049
Shibata M., 2003, ApJ, 595, 992
Shibata M., Shapiro S. L., 2002, ApJ, 572, L39–L43
Shibata M., Fujibayashi S., Lam A. T.-L., Ioka K., Sekiguchi Y., 2024, Phys. Rev. D, 109, 043051
Siegel D. M., Barnes J., Metzger B. D., 2019, Nature, 569, 241

Stanek K. Z. et al., 2003, ApJ, 591, L17
Stone J. M., Tomida K., White C. J., Felker K. G., 2020, ApJS, 249, 4
Suwa Y., Tominaga N., Maeda K., 2019, MNRAS, 483, 3607
Suzuki A., Maeda K., 2022, ApJ, 925, 148
Taddia F. et al., 2019, A&A, 621, A71
Takahashi K., Yoshida T., Umeda H., Sumiyoshi K., Yamada S., 2016, MNRAS, 456, 1320
Timmes F. X., Swesty F. D., 2000, ApJS, 126, 501
Tominaga N., 2008, ApJ, 690, 526
Tominaga N., Maeda K., Umeda H., Nomoto K., Tanaka M., Iwamoto N., Suzuki T., Mazzali P. A., 2007, ApJ, 657, L77
Ugliano M., Janka H.-T., Marek A., Arcones A., 2012, ApJ, 757, 69
Usov V. V., 1992, Nature, 357, 472
Vartanyan D., Coleman M. S. B., Burrows A., 2022, MNRAS, 510, 4689
Wang T., Vartanyan D., Burrows A., Coleman M. S. B., 2022, MNRAS, 517, 543
Woosley S. E., 1993, ApJ, 405, 273
Woosley S. E., 2010, ApJ, 719, L204
Woosley S. E., Bloom J. S., 2006, ARA&A, 44, 507
Woosley S. E., Heger A., 2006, ApJ, 637, 914
Woosley S. E., Heger A., Weaver T. A., 2002, Rev. Mod. Phys., 74, 1015
Xu D. et al., 2013, ApJ, 776, 98
Zahn J. P., 1992, A&A, 265, 115
Zhang W., Woosley S. E., Heger A., 2004, ApJ, 608, 365

APPENDIX A: ANALYSIS OF THE EFFECT OF THE OPENING ANGLE $2\theta_{\rm w}$ ON THE EJECTA PROPERTIES

In this appendix, we analyse the effect of the opening angle on the global ejecta properties. As mentioned in Section 2.3, the $\theta_{\rm w}$ is unlikely to produce significant change on the global result because the outflow expands non-relativistically, hence making the explosion configuration become quickly spherical. To confirm this, we compare the ejecta mass $M_{\rm ej}$ and the explosion energy $E_{\rm expl}$ resulting from simulations performed for the progenitor star model AD020x1.0 using three different values of the half opening angle: $\theta_{\rm w} = \pi/6\,,\ \pi/4\,,\ \pi/3$. The results are presented in Fig. A1.

Fig. A1 confirms that changes in the wind opening angle affect the final ejecta properties only slightly. As a matter of fact, $M_{\rm ej}$ differs at most by ∼19 per cent between $\theta_{\rm w} = \pi/6$ and $\theta_{\rm w} = \pi/4$ (left panel of Fig. A1) while the difference in $E_{\rm expl}$ does not exceed ∼9 per cent (between $\theta_{\rm w} = \pi/3$ and $\theta_{\rm w} = \pi/4$, see right panel of Fig. A1). In light of these results, we can conclude that varying $\theta_{\rm w}$ does not have a significant impact on the final properties of the ejecta. Therefore, given this result, the simulations outcomes of Just et al. (2022), Fujibayashi et al. (2024), Dean & Fernández (2024a) and the simplified model we employ, it is reasonable to set $\theta_{\rm w} = \pi/4$ along the equator as fiducial value for the wind injection half opening angle.

APPENDIX B: ESTIMATION OF THE TEMPERATURE THAT THE INJECTED MATTER EXPERIENCES

In this appendix, we estimate the temperature that the injected matter experiences. As the matter is assumed to be launched from the disc, we first estimate the temperature at the typical radius of the disc $r_{\rm disc}$. If the internal energy is dominated by non-relativistic particles, the temperature at the radius of the disc may be estimated from the gravitational binding energy as

$$T_{\rm nr} \sim \frac{G m_{\rm p} M_{\rm BH}}{k_{\rm B} r_{\rm disc}} \sim 2\times 10^{11}\,{\rm K}\left(\frac{M_{\rm BH}}{10\,{\rm M}_\odot}\right)\left(\frac{r_{\rm disc}}{10^8\,{\rm cm}}\right)^{-1}, \tag{B1}$$

where $m_{\rm p}$ is the proton mass and $k_{\rm B}$ is the Boltzmann's constant. On the other hand, if relativistic particles, i.e. photons and thermally generated electron–positron pairs in high temperature, are dominant in the internal energy, the temperature is obtained by solving $aT^4/\rho \sim GM_{\rm BH}/r_{\rm disc}$ as

$$T_{\rm rel} \sim \left(\frac{G\rho M_{\rm BH}}{a r_{\rm disc}}\right)^{1/4} \sim 2\times 10^{10}\,{\rm K}\left(\frac{M_{\rm BH}}{10\,{\rm M}_\odot}\right)^{1/4}\left(\frac{M_{\rm disc}}{0.1\,{\rm M}_\odot}\right)^{1/4}\left(\frac{r_{\rm disc}}{10^8\,{\rm cm}}\right)^{-1}, \tag{B2}$$

where a is the radiation constant, and the disc density is assumed to be $\rho \sim M_{\rm disc}/r_{\rm disc}^3$. The disc temperature may be the lower value of $T_{\rm nr}$ and $T_{\rm rel}$,

$$T_{\rm disc} = \min(T_{\rm nr}, T_{\rm rel}). \tag{B3}$$

We note that $M_{\rm BH}$, $M_{\rm disc}$, and $r_{\rm disc}$ are functions of time, and hence, $T_{\rm disc}$ is also a function of time.

To assess how well we estimate the disc temperature with equation (B3), we try to estimate the disc temperature with the same equation for a snapshot of the model AD35-15 in Fujibayashi et al. (2024). Fig. B1 compares the temperature along the equatorial

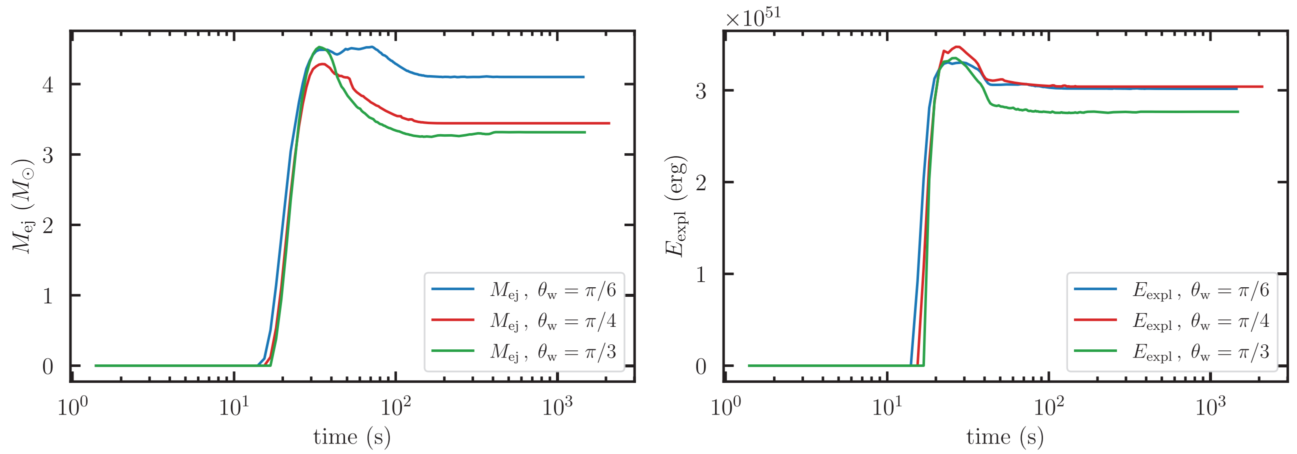

Figure A1. Evolution of $M_{\rm ej}$ (left panel) and $E_{\rm expl}$ (right panel) for the model AD020x1.0 using three different values of the half opening angle: $\theta_{\rm w} = \pi/6$ (blue line), $\theta_{\rm w} = \pi/4$ (red line), and $\theta_{\rm w} = \pi/3$ (green line).

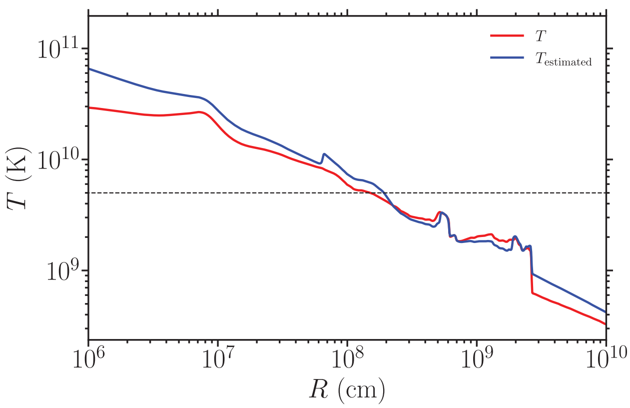

Figure B1. Temperature along the equatorial direction (red line) for the model AD35-15 in Fujibayashi et al. (2024) at $t = 10.3$ s, at which the disc outflow sets in. It is compared with the temperature estimated by equation (B3) (blue line) with the cylindrical radius R, local rest-mass density ρ, and the BH mass $\approx 16\,\mathrm{M}_\odot$ at the same time.

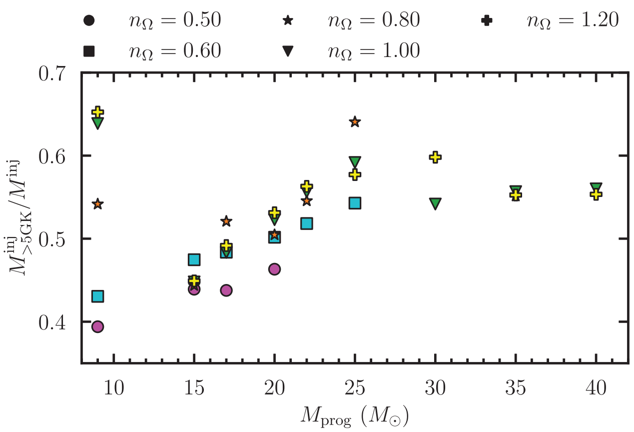

Figure B2. The ratios of the $M^{\rm inj}_{>5\,\rm GK}$ and $M^{\rm inj}$ for all the models. Markers and colours distinguish the values of n_Ω.

direction (red line) and the temperature estimated by equation (B3) with the cylindrical radius and the local rest-mass density, and the BH mass (blue line) at $t = 10.3$ s (6 s after the disc formation). This corresponds to the time at which the disc wind sets in. We find that equation (B3) estimates the actual disc temperature within a factor of two for $T \lesssim 3 \times 10^{10}$ K. Above this temperature, the neutrino emission can extract the internal energy in the disc evolution (viscous) time-scale. Thus, the temperature is lower than the estimated value. Nevertheless, as the threshold temperature for ^{56}Ni production is 5×10^9 K, we do not have to correctly estimate the disc temperature above $\sim 10^{10}$ K. We thus conclude that equation (B3) can approximate the disc temperature with good accuracy.

The mass of the injected matter that experiences temperature higher than 5 GK is then calculated as

$$M^{\rm inj}_{>5\rm GK} = \int \dot{M}_{\rm inj}(t)\Theta(T_{\rm disc}(t) - 5\,\mathrm{GK})\mathrm{d}t, \tag{B4}$$

where Θ is the Heaviside function. In Fig. B2, the ratios of $M^{\rm inj}_{>5\,\rm GK}$ and $M^{\rm inj}$ are shown for all the models of Aguilera-Dena et al. (2020). We find that about half of the injected matter experiences temperature higher than 5 GK. Thus, we may infer that a significant fraction of the injected matter is composed of ^{56}Ni (given that its electron fraction is $\sim$0.5).

APPENDIX C: EXCEPTIONAL BEHAVIOUR OF SOME MODELS

As mentioned in Section 3, we exclude some models from the analysis of the study because they showed exceptional behaviour during the simulations. The results for these simulations are listed in Table C1. In the left panel of Fig. C1, we show the distributions of the injected and explosion energy as functions of the ejecta mass for these models only, while in the right panel, we compare them to the other progenitors. From these plots, it is evident that the values of $E_{\rm inj}$, $E_{\rm expl}$, and $M_{\rm ej}$ of the excluded models do not align with those of the others. They are all progenitors with $M_{\rm prog} > 22\,\mathrm{M}_\odot$ and they present $E_{\rm inj}$ higher than expected while $E_{\rm expl}$ and $M_{\rm ej}$ lower.

The reason for this behaviour is that the matter with sufficient angular momentum inflows to the centre and forms a centrifugally supported disc *in* the computational domain ($r > r_{\rm in}$). As the matter that does not flow inside the inner boundary cannot be the energy source as an injected matter, the injected energy for such models is underestimated. This behaviour is physically inconsistent because the viscous effect is not taken into account in the computational domain. Models are regarded as physically consistent if the explosion sets in before the disc formation inside the computational domain. For such models, the injected matter pushes the stellar envelope and prevents it from inflowing into the vicinity of the inner boundary.

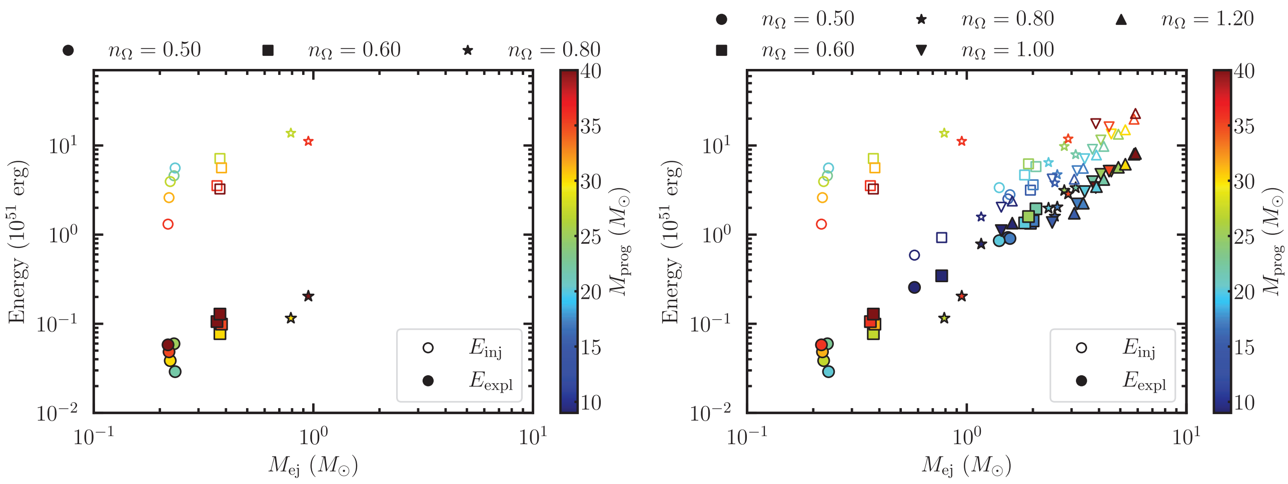

Figure C1. $E_{\rm expl}$ (filled markers) and $E_{\rm inj}$ (open markers) as functions of the ejecta mass $M_{\rm ej}$ for all the models studied in this work (left panel) and for those showing an exceptional behaviour compared to the general trend (right panel). Results for progenitors with different magnitudes of the angular velocity are distinguished by different markers, while the colour indicates the progenitor mass $M_{\rm prog}$.

Table C1. Exceptional models excluded from the analysis of the results. After the column with the model's name, from left to right, the columns list the cumulative injected energy, ejecta mass, explosion energy, average ejecta velocity, the number of tracer particles located within the ejecta, the mass of ejecta component originated from the injected matter, the ratio between the injected matter that is estimated to experience temperature higher than 5 GK and the total injected mass, the mass of ejecta component that is originated from the computational domain and experiences temperature higher than 5 GK, along with the number of tracer particles in parenthesis, the total mass of the ejecta which experiences temperature higher than 5 GK.

Model	$E_{\rm inj}$ (10^{51} erg)	$M_{\rm ej}$ (M$_\odot$)	$E_{\rm expl}$ (10^{51} erg)	$v_{\rm ej}$ (10^3 km s^{-1})	$N_{\rm p}$	$M^{\rm inj}_{\rm ej}$ (M$_\odot$)	$M^{\rm inj}_{>5\,{\rm GK}}/M^{\rm inj}$	$M^{\rm stellar}_{\rm ej,>5\,GK}$ ($N^{\rm stellar}_{\rm ej,>5\,GK}$) (M$_\odot$)	$M_{\rm ej,>5\,GK}$ (M$_\odot$)
AD022x0.5	5.59	0.22	0.03	3.53	120913	0.003	0.90	0.0230 (9791)	0.03
AD025x0.5	4.58	0.22	0.06	5.09	72916	0.001	0.56	0.00 (1)	0.00056
AD030x0.5	3.94	0.21	0.04	4.17	103540	0.004	0.89	0.03 (13151)	0.03
AD035x0.5	2.60	0.21	0.05	4.70	112094	0.002	0.82	0.05 (22152)	0.05
AD040x0.5	1.31	0.21	0.06	5.18	106482	0.003	0.81	0.041 (18387)	0.04
AD030x0.6	7.14	0.36	0.08	4.56	95468	0.006	0.91	0.10 (19466)	0.11
AD035x0.6	5.62	0.38	0.10	5.11	139220	0.005	0.86	0.10 (29247)	0.10
AD040x0.6	3.54	0.36	0.11	5.41	112656	0.002	0.84	0.10 (35565)	0.10
AD030x0.8	13.76	0.78	0.12	3.83	220315	0.007	0.90	0.16 (33604)	0.17
AD040x0.8	11.16	0.92	0.20	9.97	93655	0.008	0.89	0.34 (27650)	0.35

APPENDIX D: DEPENDENCE OF $E_{\rm expl}$ FOR THE 35 M$_\odot$ PROGENITOR

This work was motivated by our aim of better investigating the variety of explosion properties for different progenitors after the results obtained in Paper I, where we instead studied different parameters of wind injection. We expected that the variation of the progenitor mass and its angular velocity would have explained the variety of the observational data. However, as discussed in Section 3.2, our numerical results have a tighter correlation between $E_{\rm expl}$ and $M_{\rm ej}$ than that measured in by the observational data by Taddia et al. (2019) and Gomez et al. (2022) (as shown in Fig. 9). A similar strong correlation between $E_{\rm expl}$ and $M_{\rm ej}$ was also found in our previous work for the model AD020x1.0 (fig. 11 in Paper I); however the points of the distributions lie on lines with different slopes (see Fig. 9). This comparison suggests that the proportionality between $E_{\rm expl}$ and $M_{\rm ej}$ relates to the choice of the progenitor model and of the parameters for the wind injection. Therefore, we expect that fixing the progenitor model and studying its explosion varying the parameters of the wind injection, the explosion energy would distribute along a different trend for every progenitor star. To confirm our speculations, we perform additional simulations using the progenitor model AD035x1.0 and varying the parameters of the wind injections sampling some values of $t_{\rm w}$, $t_{\rm acc}$, $f_{\rm therm}$, and ξ^2 among those used in Paper I (see Section 2). The parameters used, the results for the explosion energy, the ejecta mass, and the averaged velocity are displayed in Table D1.

In Fig. D1, we show in the $E_{\rm expl}$–$M_{\rm ej}$ plane the distribution of the models with different parameters of the wind injection for the progenitor AD035x1.0 (filled markers). We also show the results obtained for the study presented in this work (see Section 3 for different progenitor models with the parameters of the wind injection fixed (orange hexagonal markers) and the outcomes obtained in Paper I with grey $\times$-markers. We additionally display the observational data from Taddia et al. (2019) and Gomez et al. (2022) (open markers) and the results obtained by Fujibayashi et al. (2024) for the same progenitor AD035x1.0.

Comparing the distribution of the explosion energy of AD035x1.0 with that of AD020x1.0, they show two slightly different trends, i.e. they lie on lines with different slopes. This supports our speculation

Table D1. Model description and key results for model M035x1.0 studied with different parameters for the wind injection. From left to right, the columns contain the wind time-scale, the ratio of the accretion and wind time-scales, the squared ratio of the asymptotic velocity of injected matter to escape velocity of the disc, the internal to kinetic energy ratio of injected matter, cumulative injected energy, ejecta mass, explosion energy, and average ejecta velocity.

Model	$t_{\rm w}$ (s)	$t_{\rm acc}/t_{\rm w}$	ξ^2	$f_{\rm therm}$	$E_{\rm inj}$ (10^{51} erg)	$M_{\rm ej}$ ($M_\odot$)	$E_{\rm expl}$ (10^{51} erg)	$v_{\rm ej}$ (10^3 km s^{-1})
M35_1_3.16_0.1_0.10	1	3.16	0.1	0.10	15.25	4.29	4.64	10.43
M35_1_10_0.1_0.10	1	10	0.1	0.10	18.06	5.53	7.45	11.63
M35_3.16_1_0.1_0.10	3.16	1	0.1	0.10	0.52	0.99	0.14	3.78
M35_3.16_3.16_0.1_0.10	3.16	3.16	0.1	0.10	16.29	4.06	4.89	11.01
M35_3.16_10_0.1_0.10	3.16	10	0.1	0.10	21.13	4.75	8.23	13.20
M35_3.16_10_0.3_0.10	3.16	10	0.3	0.10	40.20	7.82	25.02	17.94
M35_3.16_10_0.1_0.01	3.16	10	0.1	0.01	20.53	5.33	8.19	12.44
M35_10_1_0.1_0.10	10	1	0.1	0.10	1.89	1.10	0.17	3.91
M35_10_3.16_0.1_0.10	10	3.16	0.1	0.10	28.88	6.18	16.39	16.33
M35_10_3.16_0.3_0.10	10	3.16	0.3	0.10	69.53	9.48	54.25	23.99
M35_10_10_0.1_0.10	10	10	0.1	0.10	35.15	7.47	21.27	16.92
M35_10_10_0.3_0.10	10	10	0.3	0.10	88.43	9.52	72.27	27.62

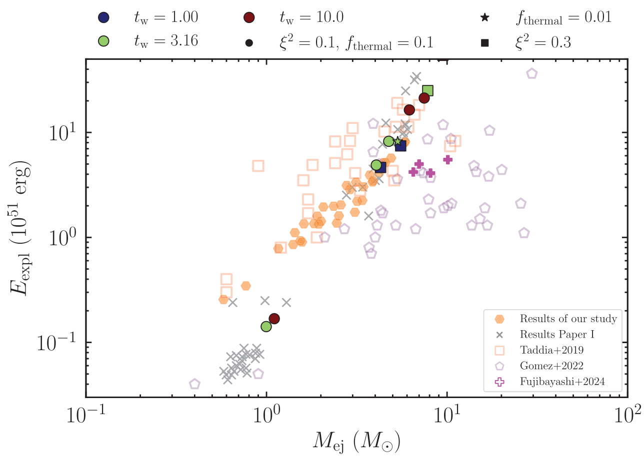

Figure D1. Wind parameter dependence of model M035x1.0 with respect to the observable pair of ejecta mass $M_{\rm ej}$ and explosion energy $E_{\rm expl}$. The colour distinguishes the wind time-scale $t_{\rm w}$. The orange hexagonal markers show the result of the study presented in this paper, while the grey x-markers represent the results obtained in Paper I for the model AD020x1.0. The open markers display the observational data for stripped-envelope SNe, some of which are Type Ic-BL SNe, taken from Taddia et al. (2019) and Gomez et al. (2022). The magenta plus-sign denotes the results obtained in a general relativistic neutrino-radiation viscous-hydrodynamics simulation with the same progenitor AD035x1.0 by Fujibayashi et al. (2024).

that by varying the progenitor structure and sophisticating the wind injection model, we may be able to reproduce a wider variety of the observational data. However it is still impossible to reproduce the observational data with $M_{\rm ej} \gtrsim 10 M_\odot$ because our choice of the progenitor models are not appropriate for this purpose.

This paper has been typeset from a TEX/LATEX file prepared by the author.